

1 **Multi-disciplinary characterizations of the Bedretto Lab**
2 **- a new underground geoscience research facility**

3 Xiaodong Ma¹, Marian Hertrich¹, Florian Amann², Kai Bröker¹, Nima Gholizadeh Doonechaly¹, Valentin
4 Gischig³, Rebecca Hochreutener¹, Philipp Kästli¹, Hannes Krietsch², Michèle Marti¹, Barbara Nägeli¹,
5 Morteza Nejati¹, Anne Obermann¹, Katrin Plenkers¹, Antonio P. Rinaldi¹, Alexis Shakas¹, Linus Villiger¹,
6 Quinn Wenning¹, Alba Zappone¹, Falko Bethmann⁴, Raymi Castilla⁴, Francisco Seberto⁴, Peter Meier⁴,
7 Thomas Driesner¹, Simon Löw¹, Hansruedi Maurer¹, Martin O. Saar¹, Stefan Wiemer¹, Domenico
8 Giardini¹

9
10 ¹Department of Earth Sciences, ETH Zürich, Zürich, 8092, Switzerland

11 ²Engineering Geology and Hydrogeology, RWTH Aachen, Aachen, 52062, Germany

12 ³CSD Ingenieure AG, Liebefeld, 3097, Switzerland

13 ⁴Geo-Energie Suisse AG, Zürich, 8004, Switzerland

14 *Correspondence to:* Xiaodong Ma (xiaodong.ma@erdw.ethz.ch)

15

16 **Abstract**

17 The increased interest in subsurface development (e.g., unconventional hydrocarbon, engineered geothermal systems (EGS),
18 waste disposal) and the associated (triggered or induced) seismicity calls for a better understanding of the hydro-seismo-
19 mechanical coupling in fractured rock masses. Being able to bridge the knowledge gap between laboratory and reservoir scales,
20 controllable meso-scale in situ experiments are deemed indispensable. In an effort to access and instrument rock masses of
21 hectometer size, the Bedretto Underground Laboratory for Geosciences and Geoenergies ('Bedretto Lab') was established in
22 2018 in the existing Bedretto Tunnel (Ticino, Switzerland), with an average overburden of 1000 m. In this paper, we introduce
23 the Bedretto Lab, its general setting and current status. Combined geological, geomechanical and geophysical methods were
24 employed in a hectometer-scale rock mass explored by several boreholes to characterize the in situ conditions and internal
25 structures of the rock volume. The rock volume features three distinct units, with the middle fault zone sandwiched by two
26 relatively intact units. The middle fault zone unit appears to be a representative feature of the site, as similar structures repeat
27 every several hundreds of meters along the tunnel. The lithological variations across the characterization boreholes manifest
28 the complexity and heterogeneity of the rock volume, and are accompanied by compartmentalized hydrostructures and
29 significant stress rotations. With this complexity, the characterized rock volume is considered characteristic of the
30 heterogeneity that is typically encountered in subsurface exploration and development. The Bedretto Lab can adequately serve
31 as a test-bed that allows for in-depth study of the hydro-seismo-mechanical response of fractured crystalline rock masses.

32

33

34 **1 Introduction**

35 The coupled hydro-seismo-mechanical characteristics of crystalline basement rock masses have traditionally been of broad
36 scientific and engineering interest. Fluid migration and circulation therein concerns rock mass permeability and transport, fault
37 instability and seismicity, and ultimately crustal strength and deformability (Achtziger-Zupančič et al., 2017)(Clauser,
38 1992)(Ingebritsen and Manning, 2010)(Manga et al., 2012)(Townend and Zoback, 2000)(Zoback and Townend, 2001). For
39 subsurface engineering development, fluid flow and the associated seismo-mechanical response need to be controllable (NRC,
40 1996). For example, in the context of engineered geothermal systems (EGS) (Tester et al., 2006)(Jordan et al., 2020), the
41 enhancement of fluid flow typically results from fracture reactivation and seismicity. Conversely, the latter needs to be
42 minimized concerning certain underground facilities (e.g., CO₂ storage, nuclear waste disposal, tunnels), in which fluid flow
43 should be regulated or even prevented (Zoback and Gorelick, 2012).

44

45 There exists a plethora of literature dedicated to the hydro-seismo-mechanical processes taking place in single fractures
46 (Goodman, 1989)(Jaeger et al., 2007)(Ye and Ghassemi, 2018) and references therein). Its fundamental mechanism has been
47 understood as the interplay between stress, permeability and seismicity. Primarily, shear and normal stress acting on the
48 fracture and the fracture's frictional property dictate its stability and seismicity, which consequently affect its hydraulic
49 aperture and permeability. Crystalline basement rock masses can often be conveniently considered as fractured systems of
50 low-porosity, lower-permeability matrix intersected by fractures of various scales with respect to permeability and
51 connectivity. However, it remains challenging to understand the hydro-seismo-mechanical processes in fractured rock masses
52 (Amann et al., 2018); and references therein), because the variability and complexity therein prevent simple upscaling from
53 single fractures.

54

55 The need to better understand the hydro-seismo-mechanical coupling in fractured rock masses becomes even more crucial in
56 the recent context of unconventional oil and gas and deep engineered geothermal systems (EGS) and the associated (triggered
57 or induced) seismicity (Cornet, 2015)(Ellsworth, 2013)(Ellsworth et al., 2016)(Giardini, 2009). At full-size reservoir scales,
58 studies on the hydro-seismo-mechanical processes have to be inferred from observations at a sparse spatial resolution (e.g.,
59 Basel, Switzerland; Cooper Basin, Australia; Cornwall, UK; Fenton Hill, USA; Helsinki, Finland; Pohang, South Korea;
60 Soultz, France). The experiments at such scales are often constrained by insufficient resolution in order to yield fundamental
61 understanding and wide application. Laboratory-scale experiments, although instrumental in revealing the fundamental
62 mechanisms, are hardly representative of the heterogeneity and complexity of natural systems such as fractured rock masses.
63 Numerical simulations, which can model the processes at various scales, offer a great opportunity to conceptually understand
64 hydro-seismo-mechanical processes but need to be calibrated against high resolution field observations.

65

66 The knowledge gap between laboratory and reservoir scales can be bridged through controllable meso-scale in situ experiments
67 (Amann et al., 2018). A handful of underground research infrastructures have been either adapted from existing mines and
68 tunnels or newly excavated (e.g., Äspö HRL, Sweden; URL, Canada; Grimsel, Switzerland; Jinping, China, Kamaishi, Japan;
69 KURT, South Korea; Mont Terri, Switzerland; Reiche Zeche, Germany; SURF, USA) (Ingraham, 2021)(Ma, 2021). The
70 exposure of the subsurface environment offers direct access to the rock masses at depth. This allows for sophisticated, multi-
71 disciplinary characterization, instrumentation and experimentation at higher spatial resolutions and more controllable scales,
72 which otherwise would not be materialized from the surface or through downhole instruments. Depending on site-specific
73 conditions, various scales (from decameter to hectometer) of rock volume can be made available for different experimental
74 purposes, offering desired heterogeneity and complexity.

75
76 While underground laboratories offer unique opportunities to access the rock masses in situ, unwanted effects are incurred.
77 The excavation inevitably perturbs the surroundings, altering the pristine rock masses and physical conditions (i.e., stress
78 changes in the near-field, pore pressure depletion, temperature perturbations) (Perras and Diederichs, 2016)(Siren et al.,
79 2015)(Tsang et al., 2005). Thus, the boundary conditions have to be understood and incorporated in the analysis.
80 Acknowledging such challenges, in situ experiments in underground laboratories remain indispensable. The efforts to approach
81 representative in situ conditions are still limited by the available rock mass scale, complexity and the burial depth.

82
83 A handful of in situ field experiments have been conducted in recent years (Fu et al., 2021)(Hertrich et al., 2021)(Ingraham,
84 2021)(Krietsch et al., 2020)(Ma, 2021)(Schoenball et al., 2020), which have significantly advanced our understanding of the
85 hydro-seismo-mechanical processes at decameter scales; however, to what extent such experiments are representative of the
86 realistic in situ heterogeneous rock mass remains an open question. As an effort to step up the scale towards hectometer rock
87 masses (Gischig et al., 2020), the Bedretto Underground Laboratory for Geosciences and Geoenergies ('Bedretto Lab'
88 hereafter) was established by ETH Zürich in 2018. The existing Bedretto Tunnel (Ticino, Switzerland) has been transformed
89 into a new underground research facility, the Bedretto Lab. Various scales of experiments will be hosted here, which are
90 pertinent to the complex geoscience and engineering issues outlined earlier. In this paper, we formally introduce the Bedretto
91 Lab, its general setting and current status. The results of a first suite of multi-disciplinary characterizations are outlined,
92 focusing on identifying a representative rock volume. Combining the characterization efforts to date, we evaluate the suitability
93 of the Bedretto Lab rock volume as a test-bed to host upcoming experiments, and offer an outlook on the challenges and
94 opportunities to advance the understanding of hydro-seismo-mechanical processes taking place in fractured crystalline rock
95 masses.

96 **2 Bedretto Lab Description**

97 The Bedretto Lab is located in the Bedretto Tunnel in the Swiss Central Alps, near the Gotthard pass region (Figure 1a). The
98 Bedretto Tunnel is 5218 m long and connects the Furka Base Tunnel in the northwest with the Bedretto Valley in the southeast
99 (Keller and Schneider, 1982). The tunnel axis runs approximately N317°E, with a gentle slope of ~0.5% dipping towards its
00 south portal. The Bedretto Tunnel was excavated as part of the construction logistics of the Furka Base Tunnel to transport the
01 muck. The elevation at Bedretto Tunnel's south portal (Tunnel Meter, TM0) and its junction with the Furka Base Tunnel is
02 1479.5 m and 1505.2 m a.s.l., respectively. Along the tunnel alignment, the rock overburden gradually rises to a maximum of
03 ~1632 m (corresponding to an elevation of 3124 m a.s.l.) at ~TM3140, then slightly decreases to ~1300 m further northwest.
04 At the location of the current Bedretto Lab (TM2000-2100), the overburden is approximately 1000 m.

05
06 The horseshoe-shaped Bedretto Tunnel was excavated by drill-and-blast with a cross-section of approximately 3 m by 3 m
07 to host rails for mucking. In some sections, the tunnel was enlarged to allow mucking trains to pass-by. Between TM2000-
08 2100, the tunnel widens into a 6 m by 3 m (width by height) niche, which was selected to host the main part of the Bedretto
09 Lab and the first suite of multi-disciplinary rock mass characterizations.

10
11 Since its completion in 1982, the Bedretto Tunnel remained largely unlined and unpaved, and was primarily used to facilitate
12 ventilation and drainage of the Furka Base Tunnel. Therefore, the rock mass structural and hydrological conditions can be
13 directly characterized, and the rock mass is accessible through relatively short boreholes. Detailed investigations carried out
14 previously focused on groundwater flow systems (Lützenkirchen, 2002)(Ofterdinger, 2001), brittle fault zone structures
15 (Lützenkirchen, 2002), localized ductile deformation and geochronology (Rast, 2020), excavation-related rock mass failure
16 (Alcaíno Olivares, 2017)(Ganye et al., 2020)(Huber, 2004)(Meier, 2017), and landslide structures (Vlasek, 2018). Since 2018,
17 the Bedretto Tunnel has been made available by its owner, Matterhorn Gotthard Bahn (MGB), to ETH Zürich for long-term
18 research, which prompted the establishment of the Bedretto Lab.

19 **2.1 Geologic and tectonic setting**

20 From its south portal, the Bedretto Tunnel consecutively penetrates metamorphic terrains of the Helvetic domain, and in
21 particular the Tremola series until TM434, the Prato series until TM1138, and the Rotondo granite until reaching its northwest
22 terminus at the Furka Base Tunnel (Keller and Schneider, 1982) (Figure 1c). The Tremola series is part of the Sasso zone,
23 which is characterized by the predominance of chlorite-mica schists and gneisses (Steiger, 1962). The Prato series is
24 characterized by amphibolites and layered biotite/quartz-feldspar gneisses in the southeast and mica/biotite gneisses and
25 migmatites from TM635 towards the northwest (Rast, 2020). The granite body that hosts the majority of the Bedretto Tunnel
26 is referred to as the Rotondo granite. The bulk composition of the Rotondo granite is primarily quartz (25-35% by volume),
27 alkali feldspar (microcline) (20-40%), plagioclase (albite and oligoclase) (10-25%) and biotite (3-8%) (Hafner, 1958)(Labhart,

28 2005). At some locations, trace amounts of mica, chlorite and garnet are encountered. The Rotondo granite is one of several
29 magmatic bodies of the Gotthard massif (Rotondo, Gamsboden, Fibbia, Cristallina and Medelser). The intrusion of the Rotondo
30 granite took place around 294 ± 1.1 Ma (Sergeev et al., 1995) in the late stages of the Variscan orogeny, and is slightly younger
31 than the Fibbia granite (299.4 ± 1.2 Ma) that intruded the Gotthard massif to the northeast (Keller et al., 1987)(Schaltegger
32 and Corfu, 1992). Ductile deformation with gneissic foliation within the Rotondo granite is generally concentrated around a
33 few shear zones (Schneider, 1985). In some sections, a weak foliation is encountered (Lützenkirchen and Loew, 2011). The
34 foliation is less pervasive than in the Fibbia granite (Schneider, 1985), where ductile shear zones are interpreted to have
35 developed as a result of progressive Alpine deformation (Marquer, 1990). However, other studies suggest that the foliation in
36 the older Fibbia granite developed during a late short-lived Variscan deformation phase that did not affect the younger Rotondo
37 granite (Mercolli et al., 1994)(Steiger and Guerrot, 1991).

38

39 The regional stress field near the Swiss Alps is not uniform and mainly affected by Alpine orogeny. The maximum horizontal
40 stress (S_{Hmax}) azimuth is generally within the SE-NW quadrant (Heidbach et al., 2018)(Kastrup et al., 2004). Based on focal
41 mechanism solutions of more than 100 earthquakes within the region between 1960 and 2000, Kastrup et al. resolved a
42 variation of the contemporary stress regime from a slight predominance of strike-slip in the Alpine foreland to a strong
43 predominance of normal faulting in the high-altitude parts of the Alps. Based on the regional S_{Hmax} orientation pattern, a ~ SE-
44 NW azimuth of S_{Hmax} is expected around the Bedretto area, which would be sub-parallel to the Bedretto Tunnel. The
45 predominance of a strike-slip stress regime and the transition towards normal faulting in high-altitude parts of the Alps implies
46 that reverse faulting is unlikely in the study area.

47 **2.2 Structural mapping**

48 Medium to large-scale fracture and fault zones (thickness ranging between sub-meters to tens of meters) are frequently visible
49 on the tunnel walls. Fabrics and mineral assemblages of brittle-ductile fault zones in the northern section of the Bedretto Tunnel
50 (between TM3500 and TM5218) have been previously mapped and analyzed in detail (Lützenkirchen, 2002)(Lützenkirchen
51 and Loew, 2011). A complementary structural mapping has recently been conducted between ~TM1140 (near the Rotondo
52 granite contact) and TM2800 (Jordan, 2019). Overall, fractures and fault zones within the Rotondo granite are mostly dipping
53 steeper than 50° and an absence of structures dipping to the east and south has been noted. Figure 2 inset shows that NE-SW
54 (tunnel-perpendicular) and N-S striking structures dominate on stereonet. In addition, E-W and SE (tunnel-parallel) sets are
55 mapped. The tunnel-perpendicular and E-W striking sets are typically more prominent and associated with a higher degree of
56 shearing, evidenced from core and outcrop observations. Structural mapping orientation results from the tunnel are consistent
57 with those from surface scanline mapping in outcrops directly above the tunnel and on aerial orthophotos (Jordan, 2019). It is
58 worth noting that the tunnel-parallel sets might be significantly undersampled (see Section 4.2 for expanded discussion).

59

60 The water inflow has also been qualitatively assessed for the fractures and fault zones between ~TM1140 and TM2800 (Jordan,
61 2019). The water inflows into the Bedretto Tunnel are primarily associated with fractures (i.e., no visible matrix porous media
62 flow) and fault zones. We observed that a few highly conductive fault zones are responsible for the majority of the bulk water
63 inflow in the tunnel. In general, the tunnel-perpendicular and E-W striking sets are associated with higher inflows. These
64 structures often contain fault cores with gouge and cataclases. As we will outline later, these two sets of structures can
65 potentially be active or be activated in a strike-slip/normal-faulting stress environment, with S_{Hmax} trending between E-W and
66 SE-NW.

67 **2.3 Preliminary in situ stress characterization**

68 Along the Bedretto Tunnel, stress-induced rock failures (e.g., spalling and kinking) frequently occur on the sidewalls, primarily
69 in tunnel sections where pre-existing fractures are hardly present. These spalling fractures do not appear to be directly induced
70 by tunnel excavation damage due to blasting. The appearance of these stress induced failures at the sidewalls suggests that the
71 horizontal stress component perpendicular to the tunnel is smaller than the vertical stress. Therefore, local reverse faulting
72 stress regime (i.e., the minor principal stress $S_3 = S_v$) is unlikely. Accordingly, S_{Hmax} corresponds to either the intermediate
73 principal stress S_2 (i.e., normal faulting, $S_1 = S_v$), or the major principal stress S_1 (i.e., strike slip, $S_2 = S_v$). Nonetheless, rotation
74 of the stress tensor is possible due to local topography (Liu and Zoback, 1992)(Meier, 2017). Given strong variations of the
75 overburden above the Bedretto Tunnel (Figure 1c), the topographic effect is in competition with the tectonics-controlled stress
76 pattern to result in significant local stress variations along the tunnel. A previous study showed that the topographic effect is
77 strong at low overburden but diminishes significantly under larger overburden (Meier, 2017).

78
79 Small scale hydraulic fracturing tests, or mini-fracs (Haimson and Cornet, 2003), were conducted between December 2018
80 and July 2019 to obtain an estimation of the in situ stress field of the rock volume between TM1750 and TM2250 (Ma et al.,
81 2020b). The tests were performed in six short (30 - 40 m long) SB boreholes ('SB' denoting stress measurement borehole),
82 avoiding major fault zones (Figure 2). On borehole televiewer logs, the observed hydraulic fractures are steeply-dipping, which
83 generally agrees with the assumption that the overburden stress is larger than the horizontal stresses and approximates a
84 principal stress direction. The inferred average direction of the maximum horizontal stress (S_{Hmax}) is approximately N100-
85 110°E. The magnitude of the overburden or vertical stress (S_v) is estimated by integrating the granite density of the overburden
86 (≈ 1030 m), which is approximately 26.5 MPa. The measured S_{hmin} magnitude is 14.6 ± 1.4 MPa, and the estimated S_{Hmax} is
87 25.4 ± 2.3 MPa (Bröker, 2019)(Bröker and Ma, 2021). Acknowledging measurement uncertainty and local stress
88 heterogeneity, the mini-frac tests indicate that the stress state in the vicinity of the Bedretto Lab is transitional between normal
89 and strike-slip faulting conditions ($S_v \geq S_{Hmax} > S_{hmin}$). This is generally consistent with the expected regional stress state
90 (Heidbach et al., 2018)(Kastrup et al., 2004), although the stress ratio at the Bedretto Lab differs significantly from that inverted
91 from deep earthquakes in the region.

92

93 From overnight pressure decay tests (the shut-in phase after the mini-frac re-opening cycle that typically lasts 13 - 15 hours)
94 in the SB borehole mini-frac intervals, the pore pressure (P_p) was measured and ranges between 2.0-5.6 MPa, considerably
95 below the expected hydrostatic pressure (7-9 MPa, (Vlasek, 2018)). This reflects the impact of tunnel drainage and pressure
96 drawdown that has been ongoing since the tunnel's excavation. Similar underpressured conditions have also been observed at
97 distances of 60 m (4 MPa) and 90 m (5 MPa) from previous research boreholes located near the Bedretto Tunnel's NW terminus
98 (Evans, K., personal communication). Although such effects diminish further away from the tunnel, studies of similar
99 underground laboratory settings suggest that cooling and drainage associated stress perturbations can still be present beyond
00 100 m from the tunnel wall (Fu et al., 2018). (Note: the ambient temperature inside the Bedretto Tunnel is $\sim 18^\circ\text{C}$ year-round.)
01 The coupled effects of excavation damage zone, cooling and drainage certainly warrant cautious interpretation of the near-
02 tunnel stress measurements (Evans et al., 2003).

03 **3 Rock volume characterizations**

04 In late 2019, three boreholes (CB1,2,3; 'CB' denotes characterization borehole) have been drilled between TM2000-2100 to
05 enable a comprehensive characterization of the Bedretto Lab rock mass volume. The lengths of sub-parallel boreholes range
06 from ~ 200 to 300 m, and penetrate the rock mass at the tunnel's southwest side wall. Figures 2 and 3 present the three-
07 dimensional view of the layout of these boreholes, in relation to the tunnel and the short SB boreholes. CB1,2,3 boreholes
08 were fully cored (with nominal borehole diameter of 97 mm and core size of approx. 63 mm). Technical details of these
09 boreholes are compiled in Table 1. The cores facilitated a geological interpretation of the rock volume (Section 3.1). A suite
10 of geophysical logging runs were conducted soon after the boreholes were drilled. Figure 4 presents a composite log of CB1
11 as an example. Geomechanical interpretation along the penetrated rock volume is complemented by discrete hydraulic
12 fracturing stress measurements at selected depth intervals in CB1 (Section 3.2). Geophysical imaging was made available
13 through ground-penetrating radar (GPR) in CB1,2,3 boreholes to illuminate the complex geological structures (Section 3.3).
14 A multi-packer system was installed in CB2 for hydraulic characterization within the complex structures (Section 3.4). We
15 also present some of the laboratory testing results conducted on samples of the host Rotondo granite to date (Section 3.5).

16 **3.1 Geological characterization**

17 The geologic characterization of the CB rock volume relies on the combination of core logging and acoustic/optical televiewer
18 logs (ATV/OTV) to identify key structures. The characterized rock volume is composed of weakly deformed Rotondo granite
19 protolith (i.e., weakly foliated), intersected by less frequently distributed, highly foliated ductile shear zones. The mylonitic
20 ductile shear zones are quartz- and biotite-rich and their contact with the protolith can be abrupt or gradual. The boreholes
21 intersect a variety of structures, such as open fractures, filled fractures, the aforementioned mylonitic ductile shear zones, dikes

22 and veins, and compositional foliation within the granite. The compilation of core description, structure typology and fault
23 zone identification are shown in Figure 5.

24
25 Open fractures are clearly visible as traces in both ATV and OTV. In the cores, open fractures are identified by mineral
26 precipitation on the fracture surfaces and in several instances vuggy porosity develops, likely due to hydrothermal alteration.
27 The filled fractures are generally dark in color, commonly filled with biotite and/or quartz, and are discrete features less than
28 1-2 mm thick. Ductile shear zones occur in varying degrees of intensity. Some mylonite to ultra-mylonites have sub-millimeter
29 foliations spanning a couple of meters in thickness or can occur as an abrupt strain localization feature of a couple to tens of
30 centimeters in thickness. The quartz (commonly smoky grey) or aplitic dikes and veins thickness ranges from less than 1 cm
31 to about 20 cm. While compositional foliation in the granite protolith is generally not visible in cores or logs, in some cases
32 the grains do align to form a weakly foliated texture at the core scale.

33
34 It appears that three distinct lithological units are present in the characterized rock volume, as revealed by the compiled core
35 descriptions in CB1-3 (Figure 5). Depending on the specific borehole, the first unit reaches to the measured depth (MD) of
36 about 60 to 120 m. This unit is characterized by dikes (mostly aplitic) and isolated shear fractures. This shallow unit of the
37 rock volume appears rather intact with less fractured and less deformed features. Deformation is significantly more intense in
38 the middle unit, between 120 and 200 m MD, where the majority of fault zones are located. These fault zones are composed
39 of multiple branches of anastomosing individual fault cores. After about 100 m of this highly fractured and highly deformed
40 unit, or below ~200 m MD, deformation seems to diminish as fault zones are fewer and thinner than in the middle unit above.
41 The fractures in this third unit are more discrete and singular as opposed to forming in swarms.

42
43 Fault zones were identified in the recovered cores as the combination of several features that indicate a considerable
44 concentration of deformation. Figure 6 shows an example from the middle fault zone unit intersected by CB1. Crackle breccias
45 and mylonites, following the fault rock classification (Woodcock and Mort, 2008), are commonly identified. Fine-grained
46 brittle fault rocks (e.g., fault gouges and cataclasites) are most probably present in the rock volume, but their poor consolidation
47 precludes an efficient core recovery. Our observation shows fault zones composed of multiple fault core branches with
48 overlapping damage zones and internal lenses of rock with little deformation. This configuration is close to the conceptual
49 model of fault zones (Faulkner et al., 2003) and differs from the single fault core model (Chester et al., 1993).

50
51 Figure 7 shows the orientations of each structure type. The most important structures in terms of cumulated deformation (lower
52 row) trend almost exclusively NE-SW. The same pattern is shown when comparing structure orientations around fault zones
53 with structures in between fault zones (Figure 5). Near the fault zones, the distribution of orientations tends to be unimodal
54 around the NE-SW direction (tunnel-perpendicular) while the rock volume in between fault zones also includes structures
55 oriented N-S and NW-SE (tunnel-parallel).

56 3.2 Geomechanical characterization

57 A few dedicated stress measurements were conducted at selected depth intervals in borehole CB1 via mini-frac tests. Mini-
58 frac tests could not be conducted within the borehole measured depth (MD) of 150-250 m, as high fracture density and borehole
59 enlargement/washouts prevented reliable packer seating and intact interval selection. The instantaneous shut-in pressures
60 (ISIPs) of the mini-frac cycles lead to reliable estimates of the least principal stress (or presumably S_{hmin}) (Figure 8a). These
61 S_{hmin} values are mostly around the frictional limit imposed by a frictional coefficient of $\mu = 0.6$ and a hydrostatic pore pressure
62 gradient. A frictional coefficient $\mu = 0.6$ is considered to be representative for granites at depth (Byerlee, 1978). Within a few
63 borehole intervals (e.g., MD = 53, 113, 133 m), the S_{hmin} magnitudes are noticeably higher than the rest. It is worth noting that
64 the measured in situ pore pressure is substantially below hydrostatic; therefore, the theoretically permitted lower bound of S_{hmin}
65 in this instance should be much below the expected values under the hydrostatic conditions.

66
67 The S_{hmin} values estimated from mini-fracs in CB1 are generally consistent with those obtained from the SB boreholes (Bröker,
68 2019)(Bröker and Ma, 2021). The average S_{hmin} values of SB borehole measurements are also depicted in Figure 8a, mostly
69 near the lower bounds of the measured values in CB1 borehole. The actual stress and pore pressure gradients based on the CB1
70 and SB boreholes measurements facilitate the estimation of the slip tendency ($T_s = \tau/\sigma_n$) and dilation tendency ($T_d = (S_1 - \sigma_n)/(S_1$
71 $- S_3)$) (Morris et al., 1996), where τ and σ_n are the shear stress and normal stress on the fracture/fault surface. The slip tendency
72 T_s values associated with the CB1 fractures do not exceed 0.4, which is generally not considered critical under the typical
73 crustal stress state.

74
75 A notable stress indicator is the occurrence of breakouts in all three CB boreholes (van Limborgh, 2020). These breakouts
76 primarily developed within the broadly defined middle fault zone unit. Only a few breakouts were observed outside this unit.
77 The depths and widths of the breakouts in CB1 are summarized in Figure 8d,e. Looking downhole, the diametrically-opposite
78 breakout pairs are systematically located around both sides of the borehole, suggesting relative strength isotropy despite weak
79 foliations. Within the middle fault zone unit, breakouts vary in width, depth and azimuth or disappear in some sections. The
80 breakouts' azimuthal rotations immediately near individual fractures are likely associated with stress perturbation due to shear
81 dislocation of fossil or active fractures/faults (Shamir and Zoback, 1992); the longer wavelength rotations spanning the entire
82 fault zone unit plausibly reflect systematic stress variation associated with the fault zone. The breakouts rotate counter-
83 clockwise (looking downhole with the top of the borehole referenced as north) by $\sim 50^\circ$ between ~ 145 m and 175 m MD, i.e.,
84 the beginning to the middle of the fault zone unit, then rotate backwards by approximately the same extent until they terminate
85 at the end of the fault zone unit (at ~ 220 m MD).

86 3.3 Geophysical imaging

87 Geophysical imaging of the Bedretto Lab rock volume consists of ground-penetrating radar (GPR) in both single-hole and
88 cross-hole configurations. The sensitivity of electromagnetic waves is affected by different rock properties, namely the
89 dielectric impedances between the host rock and faults/fractures. GPR surveys have been conducted in all three CB boreholes
90 with antenna systems of various center frequencies (20, 100, 250, 500 and 1000 MHz) and varying spacings.

91
92 The premise of GPR single-hole reflection imaging is to delineate structures that provide a contrast in dielectric properties in
93 the medium. In the Bedretto Lab rock volume, this is primarily a contrast between fractures (filled by clay minerals and/or
94 water) and the granitic host rock. Laboratory measurements on borehole cores reveal that the Rotondo granite has little to no
95 variability in dielectric properties, and is largely isotropic. The loss-tangent (phase angle between the resistive and reactive
96 components) of the dielectric constant is small, which facilitates large penetration depths. The relative dielectric permittivity
97 of the host rock ($\epsilon_r = 5.5$) does not vary significantly over the applied frequency range. As a result, single-hole reflection
98 imaging, where both transmitter and receiver antennas are in the same borehole, provides clean and repetitive data that can be
99 used to extract geometric information about the major fault zones present in the characterized rock volume. For the detailed
00 processing steps that we performed on the raw data, we refer to Shakas et al. (2020).

01
02 The electrically resistive granitic rock of the Bedretto Lab is a pristine setting for GPR reflection imaging. Figure 9 shows the
03 100 MHz reflection survey for boreholes CB1, 2 and 3. Clear reflections arising from nearby boreholes, as well as from several
04 (potentially) water-filled fractures and faults were identified. The first major fault intersects the borehole CB1 at approximately
05 145 m MD, which is consistent with the ATV/OTV logging observations. This fault provides a strong reflector that is traced
06 over several hundreds of meters. The observed thickness of the reflected structures on the GPR image correlates with their
07 areas and hydraulic apertures. A more detailed study that combines GPR reflections and televiewer observations to delineate
08 the geometry of the observed major fault, can be found in Shakas et al. (2021). By comparing televiewer observations to near-
09 borehole GPR effects, the latter study also suggests that the observed reflections are primarily due to water-filled (open)
10 structures (faults and fractures) and not to mineral-filled (closed) structures. We further notice that the GPR reflections match
11 well the assumed geometry of the major fault and can further introduce constraints on the fault geometry further away from
12 the boreholes.

13
14 The chevron type (V-shaped) pattern that the reflector (Figure 9) exhibits is a known ambiguity of borehole GPR surveys. This
15 artifact is introduced by projecting the fault/fracture plane that intersects the borehole in 3D onto 2D space (Olsson et al.,
16 1985). To overcome this issue, (Hediger, 2020) performed the correlation between the structures inferred from GPR reflections
17 and ATV/OTV data, in an effort to delineate the major fault zones and fractures. Furthermore, several diffractions can be seen

18 in the upper volume. These are most probably due to water-filled fractures/faults that are sub-perpendicular to the borehole
19 trajectory (Grasmueck et al., 2010).

20 **3.4 Hydraulic characterization**

21 Hydraulic tests were carried out in borehole CB1,2,3 to characterize their transmissivity (Münger, 2020). The connectivity
22 between different intervals/boreholes was also identified based on the measurable pressure response in one interval/borehole
23 due to injection/production in another. Borehole CB1 and CB3 were closed at the borehole mouth (open-hole). In CB2, a
24 system of multi-packers (each 1 m long) was used to effectively isolate six intervals (see Fig 3b). The CB2 intervals were
25 chosen based on the observed fracture/fault clusters from the core and logging observations (Table 2): individual fractures in
26 intervals 1 and 2, frequent occurrence of fractures in intervals 3 and 4, and fault zones/fracture zones in intervals 5&6 and 7.
27 For hydraulic characterization, constant flow rate tests were carried out in CB1 and CB3 as well as in all six intervals in CB2.
28 Before the main flow test in each interval, a short pulse test was carried out in the corresponding interval to have an initial
29 estimate of the transmissivity of that interval, based on which, the flow rate for the main test was calculated based on the
30 infinitely acting radial flow assumption in such a way to have (ideally) a maximum of 1 MPa pressure change during the
31 injection/production to minimize geomechanical effects influencing the transmissivity results. The duration of the flow test or
32 recovery period was set so that the infinitely acting radial flow is observed for 1.5 log cycle following the wellbore storage
33 effect. Repeated tests were performed in intervals 4 and 7 in CB2. All test results, including the repeated measurements, are
34 summarized in Table 2.

35
36 The estimated transmissivities for different intervals/boreholes differ by several orders of magnitude. CB1 and CB3, each
37 characterized along its full length, show the highest transmissivities ($\sim 2.1 \times 10^{-6} \text{ m}^2/\text{s}$ and $\sim 4.5 \times 10^{-7} \text{ m}^2/\text{s}$, respectively). The
38 isolated intervals in CB2 and the open boreholes (CB1 and CB3) are assumed to be under steady-state pore pressure before
39 the start of the flow tests. This assumption and therefore the estimated transmissivities of individual boreholes have to be
40 treated with caution, since these long intervals, in particular the open holes, include several conductive structures with non-
41 uniform pressure heads, which might cause some cross flow between different structures within the same test interval. . The
42 isolated intervals in CB2 can be classified into three different groups based on their increasing transmissivities: a) intervals 1
43 and 2, b) intervals 3 and 4, and c) intervals 5&6 and 7. The estimated transmissivities in CB2 intervals are consistent with the
44 geological observations. Since all three boreholes are sub-parallel, CB1 and CB3 are expected to encompass the majority of
45 the fractures/faults included in intervals 1 to 7 in CB2. As expected, the transmissivity values of CB1 and CB3 are at least as
46 high as the largest transmissivity observed within the intervals of CB2.

47
48 In order to identify major hydraulic flow pathways within the characterized rock volume, individual constant flow rate tests
49 (drawdown/buildup) were conducted in CB1 and CB3 boreholes. The pressure response was monitored in the other borehole

50 and in all CB2 intervals. The pressure response time is defined as the first notable pattern change in the pressure signal in the
51 monitoring intervals and boreholes since the drawdown/buildup. The drawdown tests were executed with a constant extraction
52 flow rate of 120 Liter/hour in CB1, and 90 Liter/hour in CB3, which resulted in a maximum pressure change of 0.2 and 0.4
53 MPa at the end of the flow period, respectively. Each drawdown test was followed by a buildup test (Note: the characterization
54 radius during the buildup test can be limited by the accuracy of the pressure gauge and the duration of prior drawdown interval
55 and flow rate (Bourdarot, 1999)). Based on the pressure decline curves, the characteristic response time between different
56 boreholes/intervals during the drawdown tests are estimated (Table 3). The flow test in CB1 did not show any boundary effect
57 at the end of the flow period, whereas CB3 showed signs of an infinite linear constant head boundary at the end of the flow
58 period.

59
60 As shown in Figures 10, during the drawdown test in CB1, all six CB2 intervals and the CB3 were hydraulically connected to
61 CB1. However, during the drawdown test in CB3, the pressure response was only observed in CB2 intervals 3, 4, 5&6 and 7
62 and in CB1. The results also show significant heterogeneity within the test volume. For example, interval 7 in CB2 shows
63 strong hydraulic connectivity to CB3, with a response time of approximately 7 min, which contrasts the pressure response time
64 of about 1 hour during CB1 drawdown. Interval 5&6, which is located immediately below interval 7 in CB2, shows a very
65 rapid hydraulic response to CB1 drawdown (less than 2 min), but a significantly delayed response to CB3 drawdown (~50
66 min). Intervals 1 and 2 in CB2 are hydraulically connected with CB1, with a response time of approximately 100 min, however
67 no hydraulic response was observed after ~180 min of drawdown in CB3. Given these observations, none of the intervals in
68 CB2 seems to exhibit comparable hydraulic connectivity with CB1 and CB3, and a systematic pattern was not identified. Based
69 on the results of the GPR surveys (Figure 9), although the presence of a major cross-cutting structure that intersects all three
70 boreholes (CB1-2-3) is evident from the survey, it is not fully comparable with the result from hydraulic tests. For example,
71 the observed major structure from Figure 9b intersects borehole CB2 at Interval 7, whereas the results from hydraulic tests
72 show strong hydraulic connection only between Intervals 5&6 in CB2 with borehole CB1, but not with CB3. This can be
73 mainly attributed to the strong heterogeneities in the reservoir volume, which causes strong anomalies in terms of hydraulic
74 properties within short distances.

75 76 **3.5 Laboratory petrophysical and mechanical characterization**

77 Based on visual inspection, the majority of the Rotondo granite exposed at the tunnel wall appears to be homogeneous and
78 isotropic. In the deeper parts of the CB boreholes, ductile shearing is apparent, suggesting physical anisotropy. Current
79 laboratory benchtop characterizations (on various petrophysical and mechanical properties) were mostly focusing on the
80 visually homogeneous core samples. The results suggest a low to moderate elastic anisotropy combined with considerable

81 non-linearity of the elastic response. Table 4 gives a list of the physical and mechanical properties of the Rotondo granite in
82 dry and water-saturated conditions. The details for these measurements are documented in David et al. (2020).

83
84 Despite its isotropic appearance and the absence of apparent fabric orientation, ultrasonic-wave velocity measurements indicate
85 that the Rotondo granite is moderately anisotropic, with the *P*-wave anisotropy factors of about 6% and 20% for dry and water-
86 saturated samples, respectively. Considerable surge in the ultrasonic-wave velocity by saturation (more than 50%), significant
87 non-linearity in the stress-strain relationship, high permeability and considerably low *P*-wave quality-factor of 4.9 (i.e., high
88 attenuation level), all suggest a highly micro-cracked structure of the Rotondo granite.

89
90 The Rotondo granite features higher permeability when unconfined, as compared to other types of known granites. The
91 permeability of Rotondo granite in the characterized Bedretto rock mass is roughly 10 times higher than that of Grimsel granite,
92 and 100 times larger than that of Westerly granite (Brace et al., 1968)(David et al., 2020)(Wenning et al., 2018). The *P*-wave
93 velocity is considerably dependent on the confinement pressure, suggesting a highly micro-cracked structure (David et al.,
94 2020). If the high micro-crack density is characteristic of the pristine Rotondo granite in situ, significant poroelastic response
95 is expected given elevated pore pressures.

96 **4 Interdisciplinary interpretations of the rock volume**

97 The multi-disciplinary characterization of the Bedretto Lab conducted so far identified a rock volume that is both scientifically
98 interesting and practically representative. The fractures and fault zones intersected by the CB boreholes inform us of the strong
99 structural complexity and spatial heterogeneity at multiple scales. This is evidenced by the individual observations within and
00 between several boreholes and different borehole intervals. Below we strive to provide an interdisciplinary interpretation of
01 the characterization results, particularly in the context of the suitability of the rock mass as a test-bed to better understand the
02 hydro-seismo-mechanical response of realistic crystalline basement rock reservoirs.

03 **4.1 Heterogeneous rock mass, representative test volume**

04 The characterized rock mass volume encompasses a multitude of features. One of the most prominent features is the middle
05 unit composed of major fault zones and sandwiched by two comparatively more intact units. Although this middle fault zone
06 unit is composed of several fault branches, it is found that these branches are generally sub-parallel to each other and form a
07 cluster (Figures 5 and 7). The whole cluster potentially traces back to the tunnel wall and coincides with the major fault zone
08 observed between TM 1950-1993 (Castilla et al., 2020). Major fault zones of this scale seem to be repeatedly present along
09 the Bedretto Tunnel for every few hundreds of meters (Schneider, 1985), and they are generally trending perpendicular to the

10 tunnel (NE-SW) and/or E-W. Therefore, the presence of the middle fault zone unit, along with the sandwiching units,
11 reasonably characterizes the rock mass that could be encountered within the Bedretto Lab.

12

13 The sandwiching units above and below the middle fault zone unit are also considered to be characteristic of the Rotondo
14 granite protolith. The two sandwiching units seem relatively homogeneous and share similar appearance, mineralogy (inferred
15 from spectral gamma logs) and physical properties (e.g., wave velocities). Their properties are also consistent with those of
16 the rock volume characterized by the SB boreholes scattered along the Bedretto Tunnel (Caspari et al., 2019)(Greenwood et
17 al., 2019). For example, the velocity profile along borehole CB1 (Figure 4) shows gradual increase of V_P and V_S with depth
18 (from ~5250 m/s and up, comparable to ~5400 m/s from the SB borehole logs and the laboratory core measurements), despite
19 the anomalies associated with the intersection of the major fault zones.

20

21 What accompanies the lithological unit variations is the stress variations along the CB boreholes. Although a more complete
22 stress profiling is yet to be conducted, the azimuthal rotation of the breakouts across the middle fault zone unit informs us of
23 the changes in stress orientations and magnitudes. The study to quantify why the breakouts only develop within the major fault
24 zone but not in other parts of the CB boreholes nor any SB boreholes is currently ongoing. Plausibly, low rock strength in the
25 fault zone (substantially lower than the intact rock core) can promote breakout development. According to our scoping analysis,
26 the breakout azimuth at ~145 m and 220 m MD in CB1 corresponds to a far-field S_{Hmax} azimuth between E-W and SE-NW
27 (Zhang and Ma, 2021), which is generally consistent with the average value of ~N110°E measured from several SB borehole
28 mini-fracs. The breakout rotation towards the middle of the major fault zone reaches ~50°, which requires substantial stress
29 rotation and reduction in relative stress difference (or stress ratio ϕ). This could only be accommodated by the gradual changes
30 in fault zone lithology and the associated rheological variations (Casey, 1980)(Faulkner et al., 2003)(Faulkner et al., 2010).

31

32 The stress orientation reversal towards the end of the middle fault zone unit indicates that it is likely to revert to the expected
33 far-field stress condition that has been characterized. The local and global rotations of the breakouts suggest various scales of
34 stress perturbations, which warrant further modeling. The stress variations simply manifest the heterogeneity and complexity
35 of the rock volume. Such convoluted lithological and stress heterogeneity are characteristic of realistic fractured rock masses,
36 and should be considered when designing and conducting hydro-seismo-mechanical experiments therein.

37 **4.2 Prevailing structures, hydraulically-conductive features**

38 The major structure sets in the Bedretto Lab rock mass are all present in the characterized rock volume. There are four
39 prevailing sets of fractures/faults identified along the Bedretto Tunnel (azimuth N317°E). All four sets of structures have been
40 intersected by characterization boreholes CB1,2,3 (azimuth N227°E). We are cognizant of potential undersampling of certain
41 structures in each mapping campaign. For example, the tunnel-parallel sets might be under-mapped along the tunnel, and

42 similarly for the NE-SW striking sets along the CB boreholes. However, this does not seem to be the case for the CB boreholes
43 (inset of Figure 2), as there are abundant structures striking \sim NE-SW ($\pm 15^\circ$), sub-parallel to or at acute angles with the borehole
44 azimuth. This is attributed to the $\sim 45^\circ$ inclination of these boreholes so that the undersampling of these steeply-dipping
45 structures is remedied to some extent. It appears that the prevailing sets of fractures/faults in the Bedretto Lab are reasonably
46 represented in the characterized rock mass volume, but a more conclusive characterization is certainly warranted potentially
47 through drilling of boreholes oriented differently from the existing CB boreholes.

48
49 As alluded to earlier, the NE-SW and E-W striking sets of fractures and fault zones appear to be the primary structures that are
50 hydraulically-conductive in the Bedretto Lab rock volume. These structures have been identified from the tunnel walls,
51 contributing to relatively higher inflow rates among other sets. This qualitative correlation is confirmed by several independent
52 lines of evidence noted in the CB borehole characterization. Coinciding with these fracture/fault sets, appreciable anomalies
53 have been identified along the thermal and electrical conductivity logging profiles (Figure 4b,c); the core samples exhibit
54 significantly higher degree of shearing; strong reflections are shown on GPR images, indicating relatively wider hydraulic
55 apertures and/or higher dielectric property. These observations all suggest that the NE-SW and E-W striking sets are the main
56 hydraulically-conductive conduits in the Bedretto Lab rock volume.

57
58 It is worth noting that the NE-SW and E-W striking sets are more favorably-oriented in the prevailing normal and/or strike-
59 slip faulting regime. Taking the measured average of N100°E S_{Hmax} azimuth, steeply-inclined structures forming acute angles
60 with respect to S_{Hmax} are generally more susceptible to slip. Quantitatively, the calculated slip tendency shown in Figure 8
61 indicates that the NE-SW and E-W striking sets are indeed associated with higher slip tendency. Although the absolute values
62 of slip tendency (< 0.4) are below the empirical frictional limits (~ 0.6) (Byerlee, 1978), the relative criticality between different
63 structure sets seems to support the first-order control of the in situ stress.

64
65 It has been generally regarded that critically-stressed fractures and faults are associated with hydraulic conductivity (Barton et
66 al., 1995)(Townend and Zoback, 2000), because the naturally-occurring hydro-shearing processes enhance and maintain
67 fracture permeability. The critically-stressed fracture concept can plausibly explain the NE-SW and E-W striking sets being
68 more hydraulically-conductive, applicable to both the tunnel-mapping and CB borehole structures. Previous field observations
69 supporting the critically-stressed fracture concept (Barton et al., 1995)(Rogers, 2003) were mainly conducted at scales of
70 several kilometers long full-size boreholes so that this first-order relationship is not heavily affected by local stress variabilities
71 that occur at smaller scales. While this might be the case for the tunnel-mapping structures, it is perhaps tenuous to justify in
72 the case of the CB structures. As already shown, strong stress variations are evident along the CB boreholes, particularly
73 around the fault zones. The local stress variations inevitably affect the slip tendency of individual fault branches. Given that
74 the fault-perturbed in situ stress state becomes less anisotropic, the slip tendency is expected to decrease, weakening the
75 critically-stressed fracture concept. The associated stress changes around the fault zone further complicate the correlation

76 between the stress criticality and fracture conductivity for individual fractures/faults. Nevertheless, it is important to take into
77 account the corresponding scale when the stress variability is concerned (Ma et al., 2020a). The applicability of the critically-
78 stressed fracture concept to the particular case here certainly warrants further study.

79

80 Alternatively, stress-controlled hydraulic-conductivity can be evaluated based on the dilation tendency (Morris et al., 1996).
81 This concept was introduced for crustal rock masses at relatively shallow depths (e.g., <1 km) (Mattila and Follin, 2019), for
82 which variations of the normal stress on the fracture/fault exert significant control on its hydraulic aperture, and consequently,
83 conductivity. The calculated dilation tendency profile along borehole CB1 (Figure 8c) shows that the main conductive
84 structures are subject to high normal stress, i.e., low dilation tendency. which makes it difficult to evaluate the applicability
85 of the dilation concept. It is ambiguous to quantify the dilation tendency of tunnel-mapping structures, as the exact stress
86 condition is unknown and subject to significant topographic variations.

87

88 Correlating stress with hydraulic conductivity assumes that the present stress state dominates. However, the high-conductivity
89 feature of certain structure sets might have already developed under the paleo-stress condition. Although the stress condition
90 has evolved, the high conductivity could still sustain until present days. If that is the case, distinguishing them from those
91 structures naturally reactivated and hydraulically-enhanced in geologically recent time would be challenging.

92

93 **4.3 Complex, compartmentalized hydro-structures**

94 Along the Bedretto Tunnel, recurring major fault zones serve as the main hydraulic conduits, channelizing fluid circulation in
95 the rock mass. Since these fault zones are generally sub-parallel, it is unknown to what extent these main conduits are
96 hydraulically connected. Preliminary hydrological and geochemical analysis indicates that water composition changes between
97 these conduits (Brixel, B., personal communication), which suggests certain degrees of hydraulic compartmentalization of the
98 whole rock mass along and across major structures. Such hydraulic compartmentalization also exists within the rock volume
99 characterized by the CB boreholes. During the drilling phase, it was reported that abrupt increases of formation pore pressure
00 and flow rate were associated with the penetration of the middle fault zone unit and branches therein (Meier, 2020).

01

02 According to our interdisciplinary observations, those fault zones in the Bedretto Lab rock volume simultaneously act as the
03 main hydraulic conduits along the fault planes and as impermeable layers across the fault planes. This is consistent with the
04 general understanding of the fault structure in that the fault core is surrounded by damage zones (Chester et al., 1993)(Faulkner
05 et al., 2003). The fault core can be relatively impermeable for cross-flow but is able to maintain overpressure and appreciable
06 flow therein (Faulkner et al., 2010). There was significant core loss and borehole enlargement when those fault zones were
07 penetrated, so only a qualitative understanding of the fault structure was possible from examining cores and borehole

08 televiewer logs (Figures 5 and 6). On the other hand, GPR profiles allowed us to infer the physical contrast between the
09 protolith and the fault zone rocks (Figure 9). Strong reflections of the fault zones due to distinct water-bearing capacity clearly
10 set themselves apart from the Rotondo granite, although recognizing the exact fault trace is challenging, which is due to the
11 inherent ambiguity of the GPR interpretation and the complexity of the intersecting fault (zone) branches.

12

13 The complexity of the major fault zones results in compartmentalized hydro-structures. Hydraulic characterization in the CB
14 rock volume revealed significant heterogeneity of hydraulic transmissivity (Table 2). Such heterogeneity is present both along
15 individual boreholes and between boreholes, depicting complicated dominant flow paths within the rock volume. The hydraulic
16 transmissivities differ by several orders of magnitude along multiple packed intervals of borehole CB2. This reflects the
17 significant discrepancy of hydraulic property between several permeable fractures/fault zones segmented by the multi-packer
18 system. An interesting observation is the asymmetric hydraulic response between both sides of CB2, i.e., a diametrically-
19 opposite behavior between the CB1-CB2 and CB3-CB2 connectivity. As suggested earlier, correlation of cores between the
20 CB boreholes suggests that the major fault zone varies in thickness and features multiple laterally-inconsistent branches
21 (Figures 5 and 6). This could explain the irregularity of spatial hydraulic compartmentalization and asymmetric hydraulic
22 response within the rock volume. The local irregularity of structure geometry and the stress perturbation associated with the
23 fault zones may also exert additional influence. A better understanding of the hydro-structures and the hydro-mechanical
24 response within the rock volume requires carefully planned tracer tests and geophysical imaging, which is beyond the scope
25 of this paper.

26 **5 Concluding remarks**

27 The Bedretto Lab has recently been established in the Swiss Central Alps on the basis of the existing Bedretto Tunnel. It serves
28 as an underground geoscience research laboratory and geoenvironmental test-bed. The Bedretto Lab represents a new initiative
29 for conducting meso-scale experiments on the crystalline rock masses and offers opportunities for international collaborations
30 (e.g., site availability and data sharing). The Bedretto Lab is now fully operational and its main granitic rock mass volume has
31 been extensively characterized via multi-disciplinary approaches. Combined geological, geomechanical, hydrogeological and
32 geophysical methods were employed in several hectometer-scale boreholes to probe the in situ conditions and internal
33 structures of the rock volume. A scientifically interesting and practically representative rock volume has been identified.

34

35 The characterized rock volume is approximately 100 m by 300 m by 100 m in size, off the southwest sidewall of the Bedretto
36 Tunnel between TM2000-2100. The rock overburden there exceeds 1000 m, and the stress environment is dominated by normal
37 and/or strike-slip faulting. The rock volume features three distinct units, with the middle fault zone sandwiched by two
38 relatively intact units. The major fault zone appears to be a representative feature of the site, as similar structures repeat every
39 several hundreds of meters along the Bedretto Tunnel. The fault zones are visible both on extracted cores and borehole imaging

40 tools. The lithological variations across the fault zone manifests the complexity and heterogeneity of the rock volume.
41 Significant variations of the hydrological and mechanical properties at various scales are evident. Pronounced stress rotations
42 across the fault zone are observed. Compartmentalized hydrostructures have been identified, which seem to be segmented by
43 the major fault zone and branches therein.

44

45 The characterized rock volume encompasses a multitude of complex features, and it approximates the representative scale and
46 heterogeneity typically encountered in subsurface exploration and development of basement rocks. The rock volume will be
47 further characterized and densely instrumented with tailored sensors. It will allow for in-depth studies of the hydro-seismo-
48 mechanical response of fractured rock masses. The characterized rock volume will host a series of customized hydraulic
49 stimulation experiments, serving as a test-bed for EGS reservoirs (referred to as the Bedretto Reservoir Project, BRP). Another
50 rock volume further down the Bedretto Tunnel will be subsequently characterized and made available, enabling sophisticated
51 fault reactivation experiments to study induced seismicity (referred to as the Bedretto Earthquake Project, BEP). These
52 upcoming experiments are full of challenges and opportunities, with the hope to bridge the current knowledge gap and offer
53 new insights.

54

55 **Code/Data availability**

56 For all data used in this study, it is available through the Bedretto Lab website (<http://www.bedrettolab.ethz.ch>) under
57 ‘Publications’ then ‘Research Data’. Since this data set is of large quantity and interdisciplinary nature, specific data requests
58 can be made to the corresponding author and the project data manager, Rebecca Hochreutener
59 (rebecca.hochreutener@erdw.ethz.ch).

60 **Author contribution**

61 All authors of this paper collectively contribute as a team of the Bedretto Underground Laboratory for Geosciences and
62 Geoenergy. The role of each team member is described here on the Bedretto Lab website. Please see through the following
63 link. <http://www.bedrettolab.ethz.ch/about/team/>

64 **Competing interests**

65 The authors declare that they have no conflict of interest.

66 **Acknowledgements**

67 The Bedretto Underground Laboratory for Geosciences and Geoenergy is an ETH infrastructure and is financed by ETH
68 Immobilien. The Bedretto Lab experiments are funded by the Swiss Federal Office of Energy (SFOE) (project VALTER), by
69 the EU Horizon 2020 (project DESTRESS), by the EU initiative Geothermica – EraNet (project ZoDrEx and project SPINE),
70 the Werner von Siemens Stiftung (project MISS) and by ERC (project FEAR). The Bedretto tunnel is property of the
71 Matterhorn Gotthard Bahnen (MGB). Help from Simone Zaugg and Shihuai Zhang on figure editing is greatly appreciated.
72 (Ye and Ghassemi, 2018)(Rudnicki and Rice, 1975)

73

74

75 **References**

- 76 Achtziger-Zupančič, P., Loew, S., and Mariéthoz, G.: A new global database to improve predictions of permeability
77 distribution in crystalline rocks at site scale, *J. Geophys. Res. Solid Earth*, 122, 3513–3539,
78 <https://doi.org/10.1002/2017JB014106>, 2017.
- 79 Alcaíno Olivares, R.: Assessing the influence of the environmental conditions on the fracture growth in the bedretto tunnel -
80 Switzerland, University of Leeds, 2017.
- 81 Amann, F., Gischig, V., Evans, K., Doetsch, J., Jalali, R., Valley, B., Krietsch, H., Dutler, N., Villiger, L., Brixel, B.,
82 Klepikova, M., Kittilä, A., Madonna, C., Wiemer, S., Saar, M. O., Loew, S., Driesner, T., Maurer, H., and Giardini, D.: The
83 seismo-hydromechanical behavior during deep geothermal reservoir stimulations: open questions tackled in a decameter-scale
84 in situ stimulation experiment, 9, 115–137, <https://doi.org/10.5194/se-9-115-2018>, 2018.
- 85 Barker, J. A.: A generalized radial flow model for hydraulic tests in fractured rock, *Water Resour. Res.*, 24, 1796–1804,
86 <https://doi.org/10.1029/WR024I010P01796>, 1988.
- 87 Barton, C. A., Zoback, M. D., and Moos, D.: Fluid flow along potentially active faults in crystalline rock, *Geology*, 23, 683–
88 686, [https://doi.org/10.1130/0091-7613\(1995\)023<0683:FFAPAF>2.3.CO;2](https://doi.org/10.1130/0091-7613(1995)023<0683:FFAPAF>2.3.CO;2), 1995.
- 89 Bourdarot, G.: Well testing: Interpretation methods, 1999.
- 90 Brace, W. F., Walsh, J. B., and Frangos, W. T.: Permeability of granite under high pressure, *J. Geophys. Res.*, 73, 2225–2236,
91 <https://doi.org/10.1029/JB073I006P02225>, 1968.
- 92 Bröker, K.: In-situ stress and rock mass characterization via mini-frac tests at the Bedretto Underground Laboratory, ETH
93 Zurich, <https://doi.org/10.3929/ethz-b-000445278>, 2019.
- 94 Bröker, K. and Ma, X.: Estimating the least principal stress in a granitic rock mass: systematic mini-frac tests and elaborated
95 pressure transient analysis, <https://doi.org/10.3929/ethz-b-000466482>, 2021.
- 96 Byerlee, J.: Friction of Rocks, in: *Rock Friction and Earthquake Prediction*, edited by: Byerlee, J. D. and Wyss, M., Birkhäuser
97 Basel, Basel, 615–626, https://doi.org/10.1007/978-3-0348-7182-2_4, 1978.
- 98 Casey, M.: Mechanics of shear zones in isotropic dilatant materials, *J. Struct. Geol.*, 2, 143–147, <https://doi.org/10.1016/0191->
99 8141(80)90044-9, 1980.
- 00 Caspari, E., Greenwood, A., Baron, L., and Holliger, K.: Wireline logging of Bedretto stress measurement boreholes -
01 preliminary results, in: *SCCER-SoE Science Report 2019*, 2019.
- 02 Castilla, R., Krietsch, H., Jordan, D., Ma, X., Serbeto, F., Shakas, A., Guntli, P., Bröker, K., Löw, S., Hertrich, M., Bethmann,
03 F., and Meier, P.: Conceptual Geological Model of the Bedretto Underground Laboratory for Geoenergies, 2020, 1–5,
04 <https://doi.org/10.3997/2214-4609.202011912>, 2020.
- 05 Chester, F. M., Evans, J. P., and Biegel, R. L.: Internal structure and weakening mechanisms of the San Andreas Fault, *J.*
06 *Geophys. Res.*, 98, 771–786, <https://doi.org/10.1029/92JB01866>, 1993.
- 07 Clauser, C.: Permeability of crystalline rocks, *Eos, Trans. Am. Geophys. Union*, 73, 233–238,

08 <https://doi.org/10.1029/91EO00190>, 1992.

09 Cornet, F. H.: Earthquakes induced by fluid injections, *Science* (80-.), 348, 1204–1205,
10 <https://doi.org/10.1126/science.aab3820>, 2015.

11 David, C., Nejati, M., and Geremia, D.: On petrophysical and geomechanical properties of Bedretto Granite, ETH Zurich,
12 <https://doi.org/10.3929/ethz-b-000428267>, 2020.

13 Ellsworth, W. L.: Injection-Induced Earthquakes, *Science* (80-.), 341, <https://doi.org/10.1126/SCIENCE.1225942>, 2013.

14 Ellsworth, D., Spiers, C. J., and Niemeijer, A. R.: Understanding induced seismicity, *Science* (80-.), 354, 1380–1381,
15 <https://doi.org/10.1126/science.aal2584>, 2016.

16 Evans, K., Dahlø, T., and Roti, J.-A.: Mechanisms of Pore Pressure-stress Coupling which Can Adversely Affect Stress
17 Measurements Conducted in Deep Tunnels, *Pure Appl. Geophys.* 2003 1605, 160, 1087–1102,
18 <https://doi.org/10.1007/PL00012562>, 2003.

19 Faulkner, D. R., Lewis, A. C., and Rutter, E. H.: On the internal structure and mechanics of large strike-slip fault zones: field
20 observations of the Carboneras fault in southeastern Spain, 367, 235–251, <https://doi.org/https://doi.org/10.1016/S0040->
21 [1951\(03\)00134-3](https://doi.org/10.1016/S0040-1951(03)00134-3), 2003.

22 Faulkner, D. R., Jackson, C. A. L., Lunn, R. J., Schlische, R. W., Shipton, Z. K., Wibberley, C. A. J., and Withjack, M. O.: A
23 review of recent developments concerning the structure, mechanics and fluid flow properties of fault zones, *J. Struct. Geol.*,
24 32, 1557–1575, <https://doi.org/10.1016/J.JSG.2010.06.009>, 2010.

25 Fu, P., White, M. D., Morris, J. P., Kneafsey, T. J., and Collab Team, E.: Predicting Hydraulic Fracture Trajectory Under the
26 Influence of a Mine Drift in EGS Collab Experiment I, *Proceedings, 43rd Work. Geotherm. Reserv. Eng.*, 1–11, 2018.

27 Fu, P., Schoenball, M., Ajo-Franklin, J. B., Chai, C., Maceira, M., Morris, J. P., Wu, H., Knox, H., Schwering, P. C., White,
28 M. D., Burghardt, J. A., Strickland, C. E., Johnson, T. C., Vermeul, V. R., Sprinkle, P., Roberts, B., Ulrich, C., Guglielmi, Y.,
29 Cook, P. J., Dobson, P. F., Wood, T., Frash, L. P., Huang, L., Ingraham, M. D., Pope, J. S., Smith, M. M., Neupane, G., Doe,
30 T. W., Roggenthen, W. M., Horne, R., Singh, A., Zoback, M. D., Wang, H., Condon, K., Ghassemi, A., Chen, H., McClure,
31 M. W., Vandine, G., Blankenship, D., Kneafsey, T. J., and Team, E. C.: Close Observation of Hydraulic Fracturing at EGS
32 Collab Experiment 1: Fracture Trajectory, Microseismic Interpretations, and the Role of Natural Fractures, *J. Geophys. Res.*
33 *Solid Earth*, e2020JB020840, <https://doi.org/10.1029/2020JB020840>, 2021.

34 Ganye, J. A., Alcaïno-Olivares, R., Perras, M. A., and Leith, K.: Back analysis to determine the stress state around the Bedretto
35 Adit, Switzerland, *ISRM Int. Symp. - EUROCK 2020*, 2020.

36 Giardini, D.: Geothermal quake risks must be faced, *Nat.* 2009 4627275, 462, 848–849, <https://doi.org/10.1038/462848a>, 2009.

37 Gischig, V. S., Giardini, D., Amann, F., Hertrich, M., Krietsch, H., Loew, S., Maurer, H., Villiger, L., Wiemer, S., Bethmann,
38 F., Brixel, B., Doetsch, J., Doonechaly, N. G., Driesner, T., Dutler, N., Evans, K. F., Jalali, M., Jordan, D., Kittilä, A., Ma, X.,
39 Meier, P., Nejati, M., Obermann, A., Plenkers, K., Saar, M. O., Shakas, A., and Valley, B.: Hydraulic stimulation and fluid
40 circulation experiments in underground laboratories: Stepping up the scale towards engineered geothermal systems, *Geomech.*
41 *Energy Environ.*, 24, 100175, <https://doi.org/10.1016/j.gete.2019.100175>, 2020.

42 Goodman, R. E.: Introduction to rock mechanics, Wiley, 562 pp., 1989.

43 Grasmueck, M., Coll, M., Eberli, G. P., and Pomar, K.: Diffraction imaging of vertical fractures and karst with full-resolution
44 3D GPR, cassis quarry, France, 72nd Eur. Assoc. Geosci. Eng. Conf. Exhib. 2010 A New Spring Geosci. Inc. SPE Eur. 2010,
45 3, 2043–2047, <https://doi.org/10.3997/2214-4609.201400841/CITE/REFWORKS>, 2010.

46 Greenwood, A., Caspari, E., Baron, L., and Holliger, K.: Borehole radar and full waveform sonic measurements of the Bedretto
47 stress-measurement boreholes, in: SCCER-SoE Science Report 2019, 2019.

48 Hafner, S.: Petrographie des südwestlichen Gotthardmassivs zwischen St.Gotthardpass und Nufenenpass, ETH Zürich, Zürich,
49 <https://doi.org/10.3929/ethz-a-000097546>, 1958.

50 Haimson, B. C. and Cornet, F. H.: ISRM Suggested Methods for rock stress estimation—Part 3: hydraulic fracturing (HF)
51 and/or hydraulic testing of pre-existing fractures (HTPF), *Int. J. Rock Mech. Min. Sci.*, 40, 1011–1020,
52 <https://doi.org/https://doi.org/10.1016/j.ijrmms.2003.08.002>, 2003.

53 Hediger, R.: 3D geological model of a shear zone conditioned on geophysical data and geological observations, ETH Zurich,
54 <https://doi.org/10.3929/ethz-b-000455004>, 2020.

55 Heidbach, O., Rajabi, M., Cui, X., Fuchs, K., Müller, B., Reinecker, J., Reiter, K., Tingay, M., Wenzel, F., Xie, F., Ziegler,
56 M. O., Zoback, M.-L., and Zoback, M.: The World Stress Map database release 2016: Crustal stress pattern across scales, 744,
57 484–498, <https://doi.org/https://doi.org/10.1016/j.tecto.2018.07.007>, 2018.

58 Hertrich, M., Brixel, B., Broeker, K., Driesner, T., Gholizadeh, N., Giardini, D., Jordan, D., Krietsch, H., Loew, S., Ma, X.,
59 Maurer, H., Nejati, M., Plenkers, K., Rast, M., Saar, M., Shakas, A., van Limborgh, R., Villiger, L., Wenning, Q. C., Ciardo,
60 F., Kaestli, P., Obermann, A., Rinaldi, A. P., Wiemer, S., Zappone, A., Bethmann, F., Castilla, R., Christe, F., Dyer, B.,
61 Karvounis, D., Meier, P., Serbeto, F., Amann, F., Gischig, V., and Valley, B.: Characterization, Hydraulic Stimulation, and
62 Fluid Circulation Experiments in the Bedretto Underground Laboratory for Geosciences and Geoenergies , 18 June 2021.

63 Horner, D. R.: Pressure Build-up in Wells , 28 May 1951.

64 Huber, B.: Stress-induced Fractures in the Deep-seated Bedretto Tunnel: Their Geological and Geomechanical Reasons., ETH
65 Zürich, 2004.

66 Ingebritsen, S. E. and Manning, C. E.: Permeability of the continental crust: dynamic variations inferred from seismicity and
67 metamorphism, 10, 193–205, <https://doi.org/10.1111/J.1468-8123.2010.00278.X>, 2010.

68 Ingraham, M. D.: Introduction to the Special Issue: Deep Underground Laboratories II (USA), *ARMA Lett.*, 1–2, 2021.

69 Jaeger, J. C., Cook, N. G. W., and Zimmerman, R.: Fundamentals of Rock Mechanics, Wiley, 488 pp., 2007.

70 Jordan, D.: Geological Characterization of the Bedretto Underground Laboratory for Geoenergies, ETH Zurich, Geological
71 Institute, <https://doi.org/10.3929/ethz-b-000379305>, 2019.

72 Jordan, T., Fulton, P., Tester, J., Bruhn, D., Asanuma, H., Harms, U., Wang, C., Schmitt, D., Vardon, P. J., Hofmann, H.,
73 Pasquini, T., and Smith, J.: Borehole research in New York State can advance utilization of low-enthalpy geothermal energy,
74 management of potential risks, and understanding of deep sedimentary and crystalline geologic systems, in: *Scientific Drilling*,
75 75–91, <https://doi.org/10.5194/sd-28-75-2020>, 2020.

76 Kastrup, U., Zoback, M. L., Deichmann, N., Evans, K. F., Giardini, D., and Michael, A. J.: Stress field variations in the Swiss
77 Alps and the northern Alpine foreland derived from inversion of fault plane solutions, *J. Geophys. Res. Earth*, 109,
78 [https://doi.org/Artn B01402](https://doi.org/Artn%20B01402) Doi 10.1029/2003jb002550, 2004.

79 Keller, F. and Schneider, T. R.: *Geologie und Geotechnik*, Schweizer Ing. und Archit., 24, 512–520, 1982.

80 Keller, F., Wanner, H., and Schneider, T. R.: *Geologischer Schlussbericht Gotthard-Strassentunnel. Beiträge zur Geologie der*
81 *Schweiz., Geotech. Ser.*, 70, 1987.

82 Krietsch, H., S. Gischig, V., Doetsch, J., F. Evans, K., Villiger, L., Jalali, M., Amann, F., and Löw, S.: Hydromechanical
83 processes and their influence on the stimulation effected volume: Observations from a decameter-scale hydraulic stimulation
84 project, 11, 1699–1729, <https://doi.org/10.5194/SE-11-1699-2020>, 2020.

85 Labhart, T.: *Erläuterungen Zum Geologischen Atlas Des Schweiz 1:25000, Val Bedretto, , Atlasblatt 68*, 2005.

86 van Limborgh, R.: Borehole Indicators of In Situ Stress Field Heterogeneity at the Bedretto Underground Laboratory, ETH
87 Zurich, <https://doi.org/10.3929/ethz-b-000445987>, 2020.

88 Liu, L. and Zoback, M. D.: The effect of topography on the state of stress in the crust: application to the site of the Cajon Pass
89 Scientific Drilling Project, *J. Geophys. Res.*, 97, 5095–5108, <https://doi.org/10.1029/91jb01355>, 1992.

90 Lützenkirchen, V.: *Structural Geology and Hydrogeology of Brittle Fault Zones in the Central and Eastern Gotthard Massif,*
91 *Switzerland, ETH Zurich*, 247 pp., <https://doi.org/10.3929/ethz-a-004522949>, 2002.

92 Lützenkirchen, V. and Loew, S.: Late Alpine brittle faulting in the Rotondo granite (Switzerland): Deformation mechanisms
93 and fault evolution, *Swiss J. Geosci.*, 104, 31–54, <https://doi.org/10.1007/s00015-010-0050-0>, 2011.

94 Ma, X.: Introduction to the Special Issue: Deep Underground Laboratories (DUL), *ARMA Lett.*, 1–2, 2021.

95 Ma, X., Saar, M. O., and Fan, L.-S.: Coulomb criterion - bounding crustal stress limit and intact rock failure: Perspectives,
96 *Powder Technol.*, 374, 106–110, <https://doi.org/https://doi.org/10.1016/j.powtec.2020.07.044>, 2020a.

97 Ma, X., Gholizadeh Doonechaly, N., Hertrich, M., Gischig, V., and Klee, G.: Preliminary in situ stress and fractures
98 characterization in the Bedretto Underground Laboratory, Swiss Alps: implications on hydraulic stimulation,
99 <http://hdl.handle.net/20.500.11850/379325>, 2020b.

00 Manga, M., Beresnev, I., Brodsky, E. E., Elkhoury, J. E., Elsworth, D., Ingebritsen, S. E., Mays, D. C., and Wang, C.-Y.:
01 Changes in permeability caused by transient stresses: Field observations, experiments, and mechanisms, *Rev. Geophys.*, 50,
02 <https://doi.org/10.1029/2011RG000382>, 2012.

03 Marquer, D.: Structures et déformation alpine dans les granités hercyniens du massif du Gothard (Alpes centrales suisses),
04 *Eclogae Geol. Helv.*, 83, 77–97, 1990.

05 Mattila, J. and Follin, S.: Does In Situ State of Stress Affect Fracture Flow in Crystalline Settings?, *J. Geophys. Res. Solid*
06 *Earth*, 124, 5241–5253, <https://doi.org/https://doi.org/10.1029/2018JB016791>, 2019.

07 Meier, M.: Geological characterisation of an underground research facility in the Bedretto tunnel, ETH Zurich, Zurich,
08 <https://doi.org/10.3929/ethz-b-000334001>, 2017.

09 Meier, M.: Heat Dilution Testing in Deep Underground Excavations, ETH Zurich, <https://doi.org/10.3929/ETHZ-B->

10 000447153, 2020.

11 Mercolli, I., Biino, G. G., and Abrecht, J.: The lithostratigraphy of the pre-Mesozoic basement of the Gotthard Massif: a
12 review, *Schweizerische Mineral. und Petrogr. Mitteilungen*, 74, 29–40, 1994.

13 Morris, A., Ferrill, D. A., and Henderson, D. B.: Slip-tendency analysis and fault reactivation, *Geology*, 24,
14 [https://doi.org/10.1130/0091-7613\(1996\)024<0275:STAAFR>2.3.CO;2](https://doi.org/10.1130/0091-7613(1996)024<0275:STAAFR>2.3.CO;2), 1996.

15 Münger, A.: Hydraulic Backbone of CB1 to CB3 Boreholes in the Bedretto Underground Lab, [https://doi.org/10.3929/ethz-b-](https://doi.org/10.3929/ethz-b-000469250)
16 000469250, 2020.

17 NRC, N. R. C.: *Rock Fractures and Fluid Flow: Contemporary Understanding and Applications*, The National Academies
18 Press, Washington, DC, <https://doi.org/10.17226/2309>, 1996.

19 Offerdinger, U. S.: Ground water flow systems in the Rotondo Granite, Central Alps (Switzerland), ETH Zürich,
20 <https://doi.org/10.3929/ethz-a-004218089>, 2001.

21 Olsson, O., Falk, L., Forslund, O., Lundmark, L., and Sandberg, E.: Investigations of Fracture Zones in Crystalline Rock by
22 Borehole Radar, *MRS Online Proc. Libr.* 1985 501, 50, 145–154, <https://doi.org/10.1557/PROC-50-145>, 1985.

23 Perras, M. A. and Diederichs, M. S.: Predicting excavation damage zone depths in brittle rocks, *J. Rock Mech. Geotech. Eng.*,
24 8, 60–74, <https://doi.org/10.1016/j.jrmge.2015.11.004>, 2016.

25 Rast, M.: *Geology, Geochronology and Rock Magnetism Along Bedretto Tunnel (Gotthard Massif, Central Alps) and*
26 *Numerical Modelling of Quartz-Biotite Aggregates*, ETH Zurich, <https://doi.org/10.3929/ETHZ-B-000454117>, 2020.

27 Renard, P.: Hytool: an open source matlab toolbox for the interpretation of hydraulic tests using analytical solutions, *J. Open*
28 *Source Softw.*, 2, 441, <https://doi.org/10.21105/JOSS.00441>, 2017.

29 Rogers, S. F.: Critical stress-related permeability in fractured rocks, *Geol. Soc. London, Spec. Publ.*, 209, 7–16,
30 <https://doi.org/10.1144/GSL.SP.2003.209.01.02>, 2003.

31 Rudnicki, J. W. and Rice, J. R.: Conditions for the localization of deformation in pressure-sensitive dilatant materials, *J. Mech.*
32 *Phys. Solids*, 23, 371–394, [https://doi.org/10.1016/0022-5096\(75\)90001-0](https://doi.org/10.1016/0022-5096(75)90001-0), 1975.

33 Schaltegger, U. and Corfu, F.: The age and source of late Hercynian magmatism in the central Alps: evidence from precise U-
34 Pb ages and initial Hf isotopes, *Contrib. to Mineral. Petrol.*, 111, 329–344, <https://doi.org/10.1007/BF00311195>, 1992.

35 Schneider, T. R.: *Basistunnel Furka—Geologische Aufnahme des Fensters Bedretto*, 1985.

36 Schoenball, M., Ajo-Franklin, J. B., Blankenship, D., Chai, C., Chakravarty, A., Dobson, P., Hopp, C., Kneafsey, T., Knox,
37 H. A., Maceira, M., Robertson, M. C., Sprinkle, P., Strickland, C., Templeton, D., Schwering, P. C., Ulrich, C., and Wood, T.:
38 Creation of a Mixed-Mode Fracture Network at Mesoscale Through Hydraulic Fracturing and Shear Stimulation, *J. Geophys.*
39 *Res. Solid Earth*, 125, e2020JB019807, <https://doi.org/10.1029/2020JB019807>, 2020.

40 Sergeev, S. A., Meier, M., and Steiger, R. H.: Improving the resolution of single-grain U/Pb dating by use of zircon extracted
41 from feldspar: Application to the Variscan magmatic cycle in the central Alps, *Earth Planet. Sci. Lett.*, 134, 37–51,
42 [https://doi.org/https://doi.org/10.1016/0012-821X\(95\)00105-L](https://doi.org/https://doi.org/10.1016/0012-821X(95)00105-L), 1995.

43 Shakas, A., Maurer, H., Giertzuch, P. L., Hertrich, M., Giardini, D., Serbeto, F., and Meier, P.: Permeability Enhancement

44 From a Hydraulic Stimulation Imaged With Ground Penetrating Radar, *Geophys. Res. Lett.*, 47, e2020GL088783,
45 <https://doi.org/10.1029/2020GL088783>, 2020.

46 Shakas, A., Wenning, Q., Krietsch, H., Hertrich, M., Giardini, D., Wiemer, S., and Maurer, H.: Modeling complex fault
47 geometry by combining single-hole GPR and televiewer information, 2021.

48 Shamir, G. and Zoback, M. D.: Stress orientation profile to 3.5 km depth near the San Andreas Fault at Cajon Pass, California,
49 *J. Geophys. Res.*, 97, <https://doi.org/10.1029/91JB02959>, 1992.

50 Siren, T., Kantia, P., and Rinne, M.: Considerations and observations of stress-induced and construction-induced excavation
51 damage zone in crystalline rock, *Int. J. Rock Mech. Min. Sci.*, 73, 165–174, <https://doi.org/10.1016/j.ijrmms.2014.11.001>,
52 2015.

53 Steiger, C. and Guerrot, R.: Variscan granitoids of the Gotthard massif, Switzerland: U–Pb single zircon and Sr–Nd data, 3,
54 1991.

55 Steiger, R. H.: Petrographie und Geologie des südlichen Gotthardmassivs zwischen St.Gotthard- und Lukmanierpass,
56 <https://doi.org/10.3929/ETHZ-A-000090198>, 1962.

57 Tester, J. W., Anderson, B. J., Batchelor, A. S., Blackwell, D. D., DiPippo, R., Drake, E. M., Garnish, J., Livesay, B., Moore,
58 M. C., Nichols, K., and others: The future of geothermal energy-Impact of enhanced geothermal systems (EGS) on the United
59 States in the 21st century: An assessment, Idaho Falls Idaho Natl. Lab., 1e8, 2006.

60 Theis, C.: The relation between the lowering of the Piezometric surface and the rate and duration of discharge of a well using
61 ground-water storage, *Eos, Trans. Am. Geophys. Union*, 16, 519–524,
62 <https://doi.org/https://doi.org/10.1029/TR016i002p00519>, 1935.

63 Townend, J. and Zoback, M. D.: How faulting keeps the crust strong, *Geology*, 28, 399–402, [https://doi.org/Doi 10.1130/0091-
64 7613\(2000\)28<399:Hfktes>2.0.Co;2](https://doi.org/Doi%2010.1130/0091-7613(2000)28%399:Hfktes%2.0.Co;2), 2000.

65 Tsang, C. F., Bernier, F., and Davies, C.: Geohydromechanical processes in the Excavation Damaged Zone in crystalline rock,
66 rock salt, and indurated and plastic clays - In the context of radioactive waste disposal, *Int. J. Rock Mech. Min. Sci.*, 42, 109–
67 125, <https://doi.org/10.1016/j.ijrmms.2004.08.003>, 2005.

68 Vlasek, A.: Deep structures of large toppling slopes at the Bedretto Adit (Ticino, Switzerland), ETH Zürich, 2018.

69 Wenning, Q. C., Madonna, C., De Haller, A., and Burg, J. P.: Permeability and seismic velocity anisotropy across a ductile-
70 brittle fault zone in crystalline rock, 9, 683–698, <https://doi.org/10.5194/SE-9-683-2018>, 2018.

71 Woodcock, N. H. and Mort, K.: Classification of fault breccias and related fault rocks, *Geol. Mag.*, 145, 435–440,
72 <https://doi.org/10.1017/S0016756808004883>, 2008.

73 Ye, Z. and Ghassemi, A.: Injection-Induced Shear Slip and Permeability Enhancement in Granite Fractures, *J. Geophys. Res.*
74 *Solid Earth*, 123, 9009–9032, <https://doi.org/10.1029/2018JB016045>, 2018.

75 Zhang, S. and Ma, X.: How Does In Situ Stress Rotate Within a Fault Zone? Insights From Explicit Modeling of the Frictional,
76 Fractured Rock Mass, *J. Geophys. Res. Solid Earth*, 126, e2021JB022348, <https://doi.org/10.1029/2021JB022348>, 2021.

77 Zoback, M. D. and Gorelick, S. M.: Earthquake triggering and large-scale geologic storage of carbon dioxide, *Proc. Natl.*

78 Acad. Sci., 109, 10164–10168, <https://doi.org/10.1073/PNAS.1202473109>, 2012.

79 Zoback, M. D. and Townend, J.: Implications of hydrostatic pore pressures and high crustal strength for the deformation of
80 intraplate lithosphere, 336, 19–30, [https://doi.org/10.1016/S0040-1951\(01\)00091-9](https://doi.org/10.1016/S0040-1951(01)00091-9), 2001.

81

82

83

84 **Tables**

85

86 Table 1. List of characterization boreholes and measurements conducted therein.

Borehole #	Location (TM)	Diameter (mm)	Length (m)	Inclination (degree)	Logging performed	Additional tests
CB1	2050	97	303	45	ATV, OTV, GPR, CAL, Cond., DEV, FWS, SGAM, Temp.	Mini-frac
CB2	2043	97	220	40	ATV, OTV, GPR, CAL, Cond., SGAM, Temp.	Pressure monitoring
CB3	2037	97	192	50	ATV, OTV, GPR, CAL, Cond., SGAM, Temp.	

87 Note:

88 1. All borehole azimuths are oriented N133°W. The nominal borehole diameter is based on the 97 mm coring bit; the actual
89 borehole diameters slightly exceed 97 mm, and vary with the coring scheme.90 2. ATV/OTV: Acoustic/Optical televiewer; GPR: Ground-penetrating radar; CAL: Caliper; Cond.: Electrical conductivity;
91 DEV: deviation tool; FWS: Full-waveform sonic; SGAM: Spectral Gamma; Temp.: Temperature.

92

93

94
95
96
97

Table 2. Single-hole Hydraulic Test Results

Interval / Borehole #	Interval Depth (MD) (m)	Interval / Borehole Length (m)	Test Date (in 2020) (mm.dd)	Transmissivity (m ² /s)				Initial Pressure (MPa)
				<i>(Theis, 1935)</i>		<i>GRF (Barker, 1988)</i>		
				<i>Drawdown</i>	<i>Buildup</i>	<i>Drawdown</i>	<i>Buildup</i>	
CB1	-	303	03.14	1.5·10 ⁻⁶	1.4·10 ⁻⁶	2.8·10 ⁻⁶	2.2·10 ⁻⁶	4.02
CB3	-	192	03.13	4.1·10 ⁻⁷	4.0·10 ⁻⁷	5.7·10 ⁻⁷	3.7·10 ⁻⁷	4.05
CB2	intervals							
1	199.8-221.8	22.2	03.07	1.4·10 ⁻¹⁰	1.4·10 ⁻¹⁰	8.7·10 ⁻¹¹	8.3·10 ⁻¹¹	4.04
2	196.8-198.3	2.0	03.12	4.1·10 ⁻¹¹	4.4·10 ⁻¹¹	1.4·10 ⁻¹¹	1.2·10 ⁻¹¹	4.06
3	177.2-195.2	18.5	03.05	1.1·10 ⁻⁸	8.4·10 ⁻⁹	8.6·10 ⁻⁹	6.9·10 ⁻⁹	3.90
4	167.7-175.7	9.5	03.09	1.4·10 ⁻⁸	1.5·10 ⁻⁸	9.5·10 ⁻⁹	4.9·10 ⁻⁹	3.94
4	-	9.5	03.11	1.7·10 ⁻⁸	1.3·10 ⁻⁸	2.0·10 ⁻⁹	5.4·10 ⁻⁹	3.97
4	-	9.5	03.11	1.2·10 ⁻⁸	1.2·10 ⁻⁸	4.8·10 ⁻⁹	3.4·10 ⁻⁹	3.98
5&6	141.7-165.2	24.1	03.11	8.4·10 ⁻⁸	8.5·10 ⁻⁸	1.3·10 ⁻⁷	4.1·10 ⁻⁸	3.99
7	125.1-140.1	15.5	03.03	2.1·10 ⁻⁷	1.8·10 ⁻⁷	5.4·10 ⁻⁸	4.6·10 ⁻⁸	3.62
7	-	15.5	03.06	1.2·10 ⁻⁷	2.0·10 ⁻⁷	2.7·10 ⁻⁸	4.2·10 ⁻⁸	3.67

98
99
00
01
02
03
04
05
06
07

Note:

1. The packer between intervals 5 and 6 did not provide proper sealing, resulting in a direct hydraulic connection between the two intervals. Thus, the interconnected intervals 5 and 6 are considered a single interval, i.e., ‘interval 5&6’.
2. Pressure measurements were conducted at the tunnel floor. Thus, the hydrostatic heads at the (center of the) interval depth are subtracted from the reported pressure values.
3. The analysis of the transient pressure curves was carried out with the MATLAB Toolbox ‘hytool’ (Renard, 2017). The tests were analyzed with two models, Theis (1935) and Generalized Radial Flow (GRF) (Barker, 1988).
4. The initial pressures of the boreholes/intervals were also determined with Horner (1951) plots and linear fitting.

08

09

10 Table 3. Characteristic pressure response time in the monitored boreholes/intervals during the drawdowns

Interval/Borehole #	Response time (hh:mm:ss) during the drawdown in	
	CB1	CB3
CB1	-	00:44:54
CB3	00:56:42	-
CB2 intervals		
1	01:41:42	-
2	01:14:48	-
3	00:26:47	02:08:24
4	00:07:02	00:50:54
5&6	00:01:55	00:51:54
7	05:16:42	00:06:38

11

12

13

14

15

16 Table 4. Selected physical properties of the Rotondo granite (measured under no confining stress)

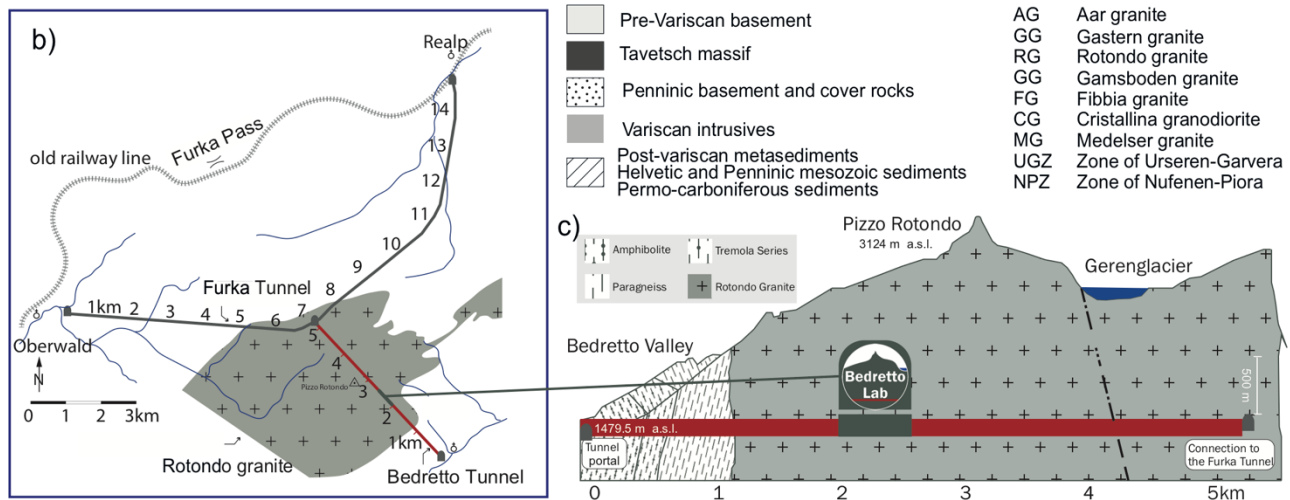
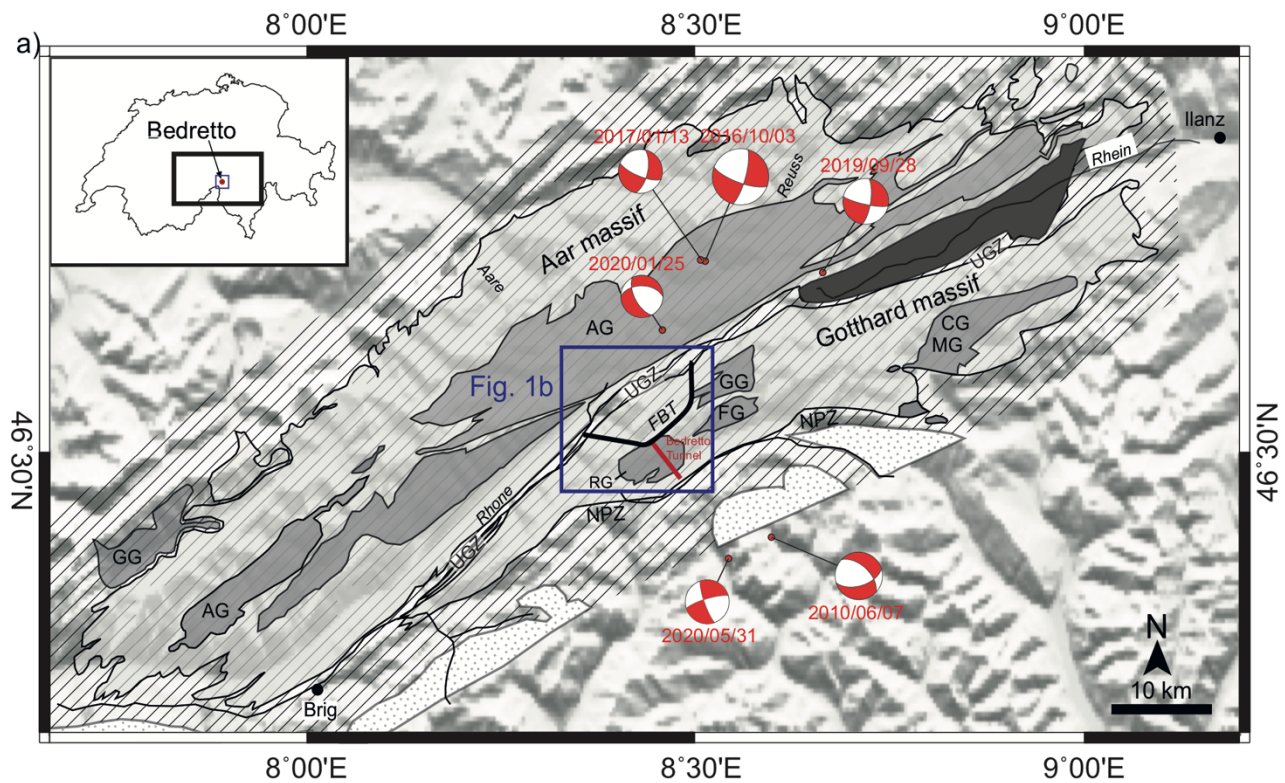
Property	Specification (unit)	Dry	Water-saturated
Porosity	connected (%)	1.36	-
	total (%)	1.75	-
Density	grain (kg/m ³)	2653	-
	bulk (kg/m ³)	2606	2620
Ultrasonic velocity	<i>P</i> -wave, V_P (km/s)	3510	5434
	<i>S</i> -wave, V_S (km/s)	1785	2526
Elastic modulus (dynamic)	Young's modulus (GPa)	22.6	45.9
	bulk modulus (GPa)	27.3	60.5
	shear modulus (GPa)	8.3	16.8
	Poisson's ratio	0.36	0.37
Permeability	(μ D)	-	4.35
Tensile strength	Brazilian Test (MPa)	8	-
Compressive strength	Uniaxial (MPa)	172	-
Fracture toughness	Mode I (tensile) (MPa·m ^{1/2})	1.3	-
	Mode II (shear) (MPa·m ^{1/2})	4	-

17

18

19

20



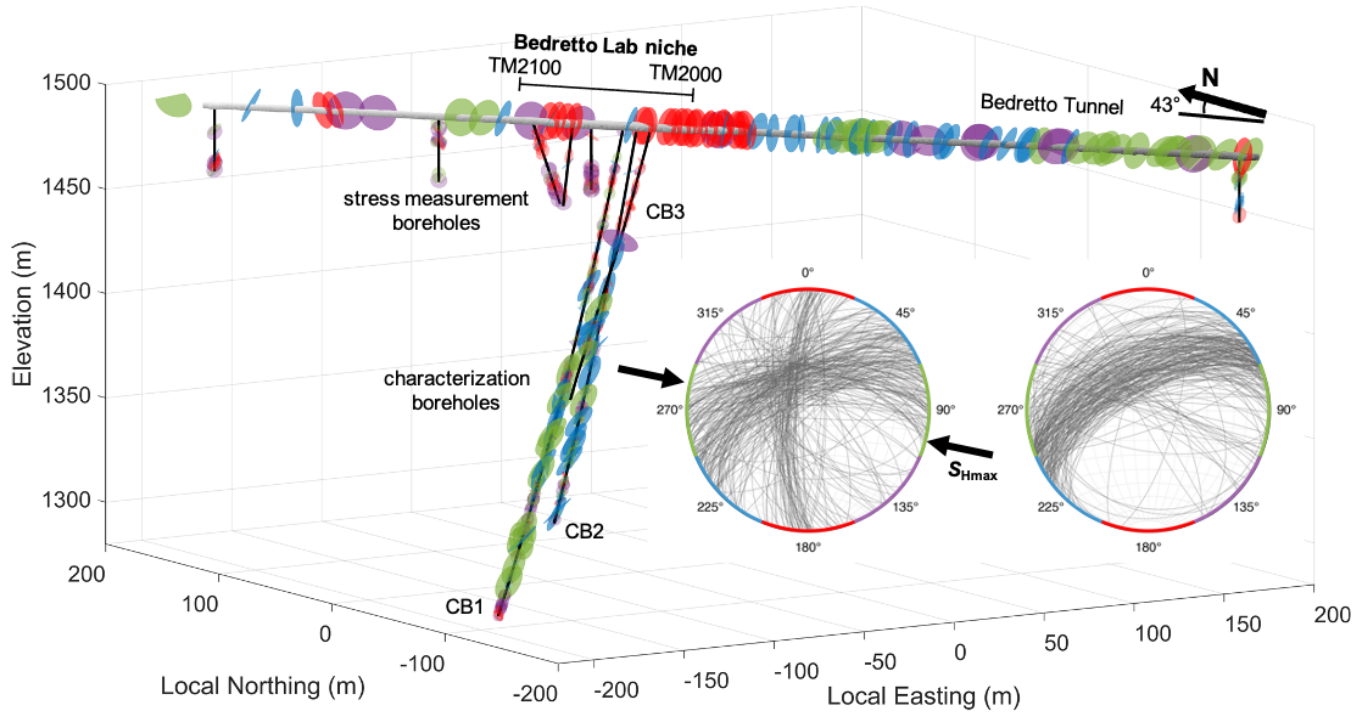
21

22 **Figure 1: a) Integrated geological, topographical and seismological information near the Aar and Gotthard massif surrounding the**
 23 **Bedretto Lab (Keller and Schneider, 1982; adapted from Lützenkirchen and Loew, 2011, and Gischig et al., 2020). b) Map view of**
 24 **the Bedretto Tunnel and the hosting Rotondo granite. c) Cross-sectional view of the Bedretto Lab with respect to the tunnel.**

25

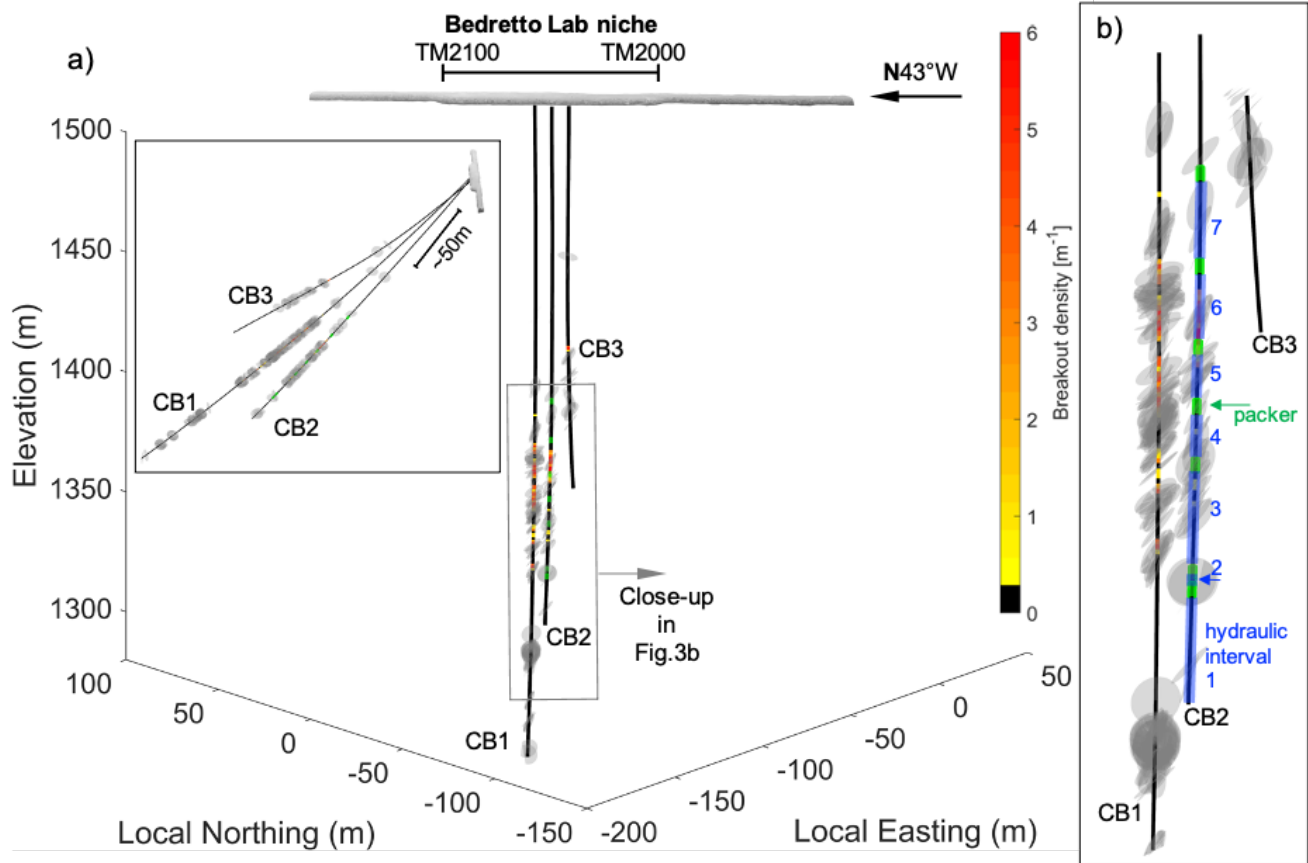
26

27
28



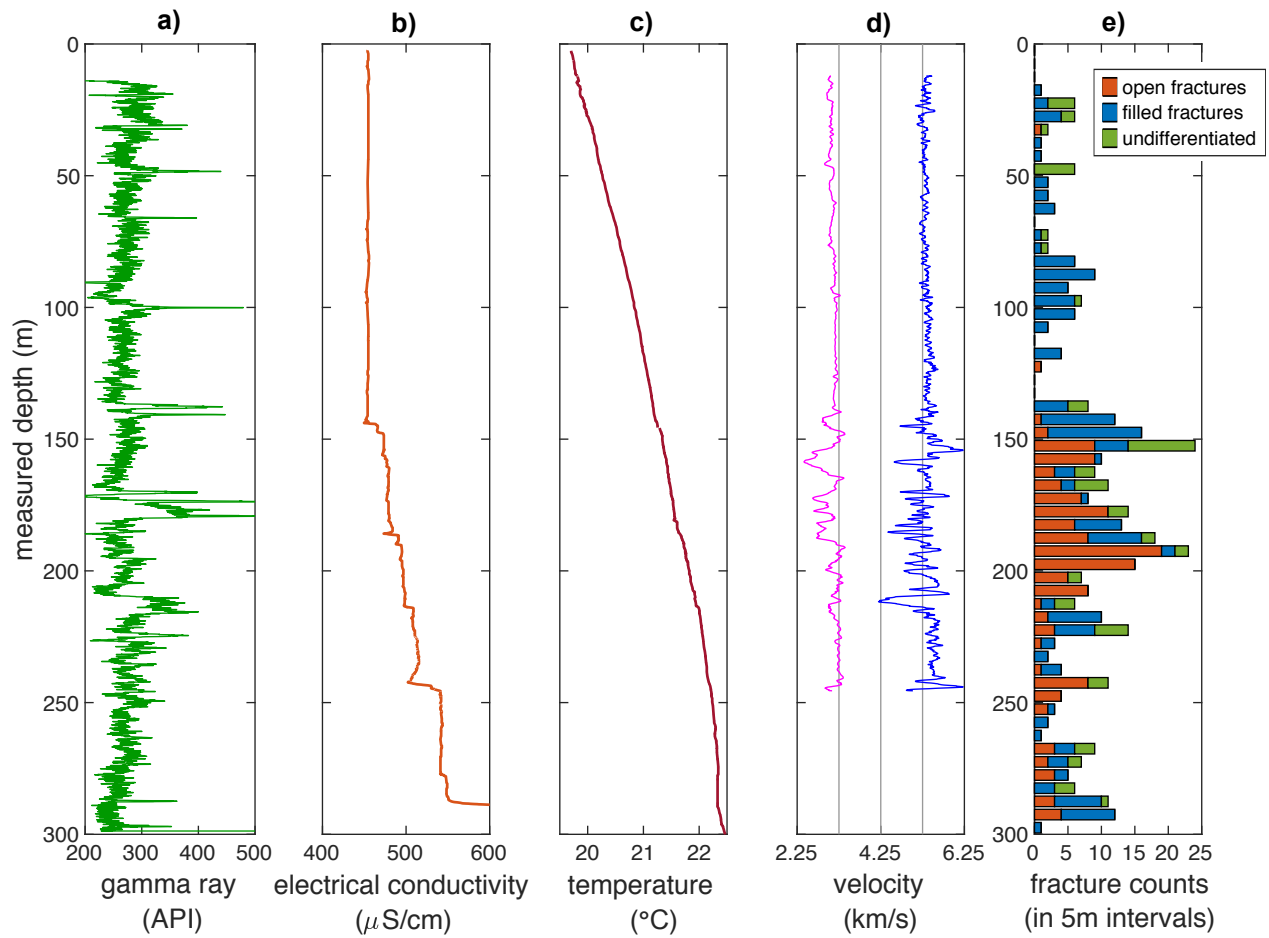
29
30
31
32
33
34
35
36

Figure 2: Configuration of the CB1,2,3 boreholes with respect to the Bedretto Tunnel. Fractures and fault zones, mapped along the tunnel and the boreholes, are colored with respect to their strikes. Stress measurement boreholes (SB) are also shown. Inset: Stereonet of fractures and fault zones mapped along the tunnel (left) and the CB1,2,3 boreholes (right) (only structures represented in the lower row of Figure 7), respectively. The four fracture/fault sets are colored distinctly according to their strikes, which is also marked on the circumference of the stereonets.



37
38
39
40
41
42
43
44

Figure 3: Configuration of boreholes CB1,2,3 and the mapped major fractures/fault zones therein. a) Looking down approximately normal to the three boreholes. Inset shows the side view of the boreholes. b) Close-up of the major fault zone interval. Note the breakout density along the CB borehole major fault zone and the multi-packer system (and the divided hydraulic intervals) installed in CB2 (see Table 2 for details).

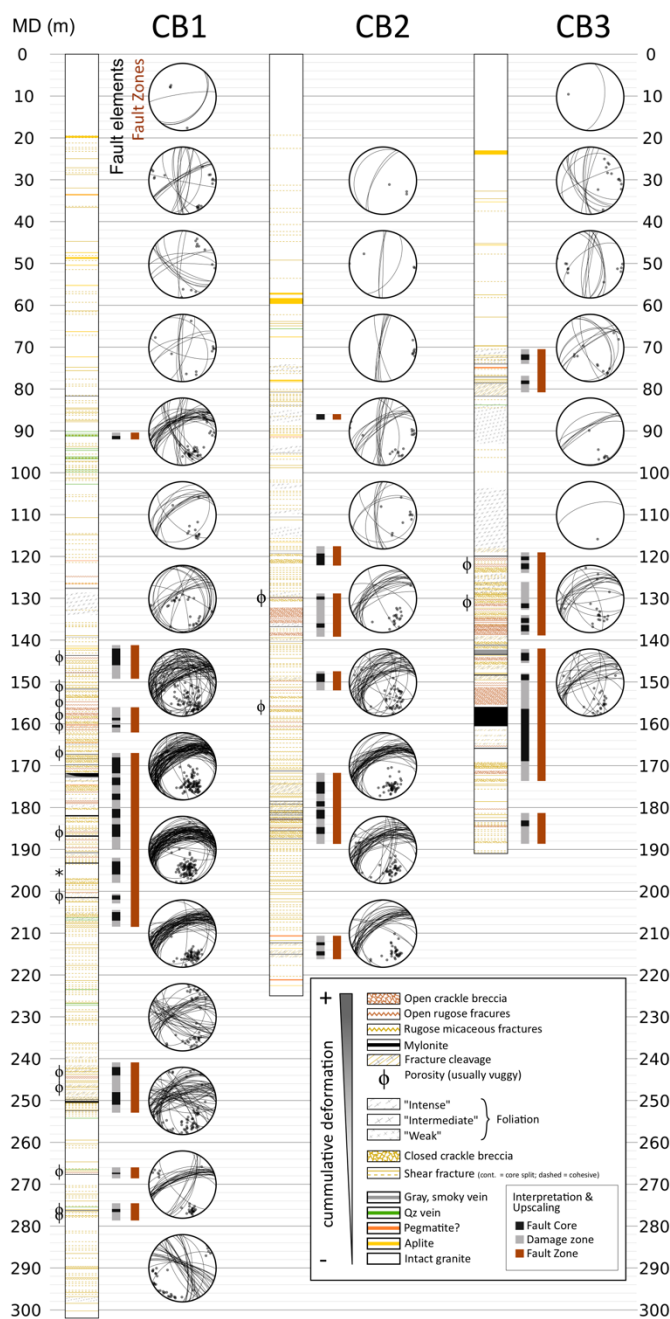


46 **Figure 4: Integrated geophysical logs of borehole CB1: a) gamma ray; b) electrical conductivity; c) temperature; d) sonic**
 47 **compressional and shear wave velocities (V_p and V_s); e) density of mapped fractures from televiewer logs.**

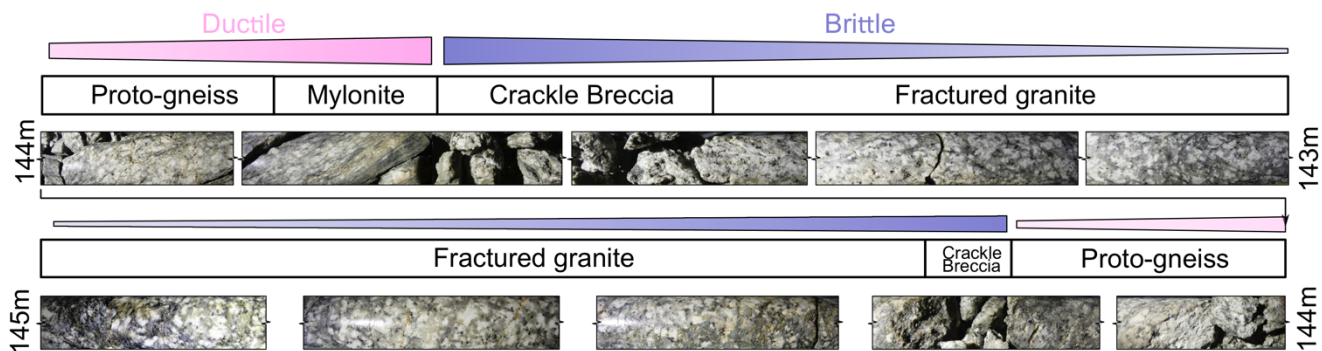
48

49

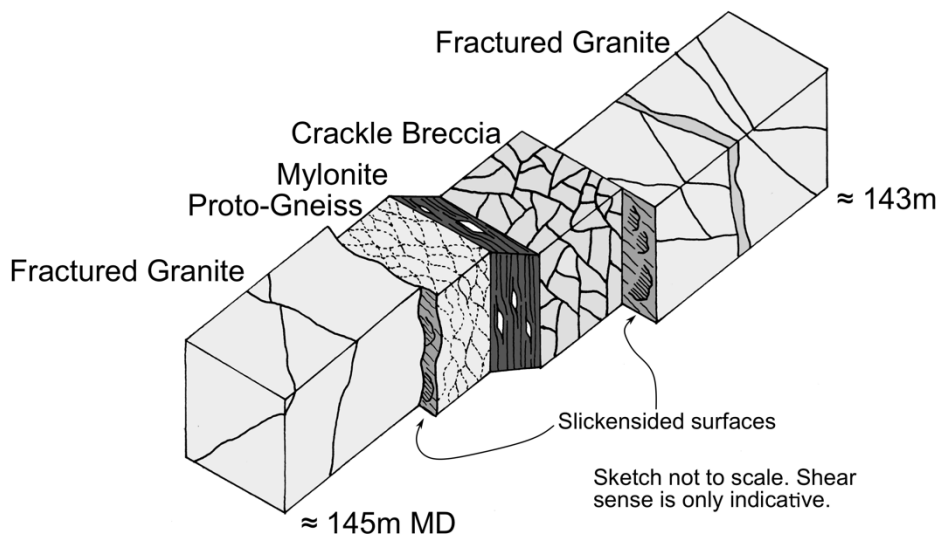
50



52 **Figure 5: Core description showing the geological designations and structural orientations (measured by the acoustic and optical**
 53 **televiwers, i.e., ATV/OTV).**



a)



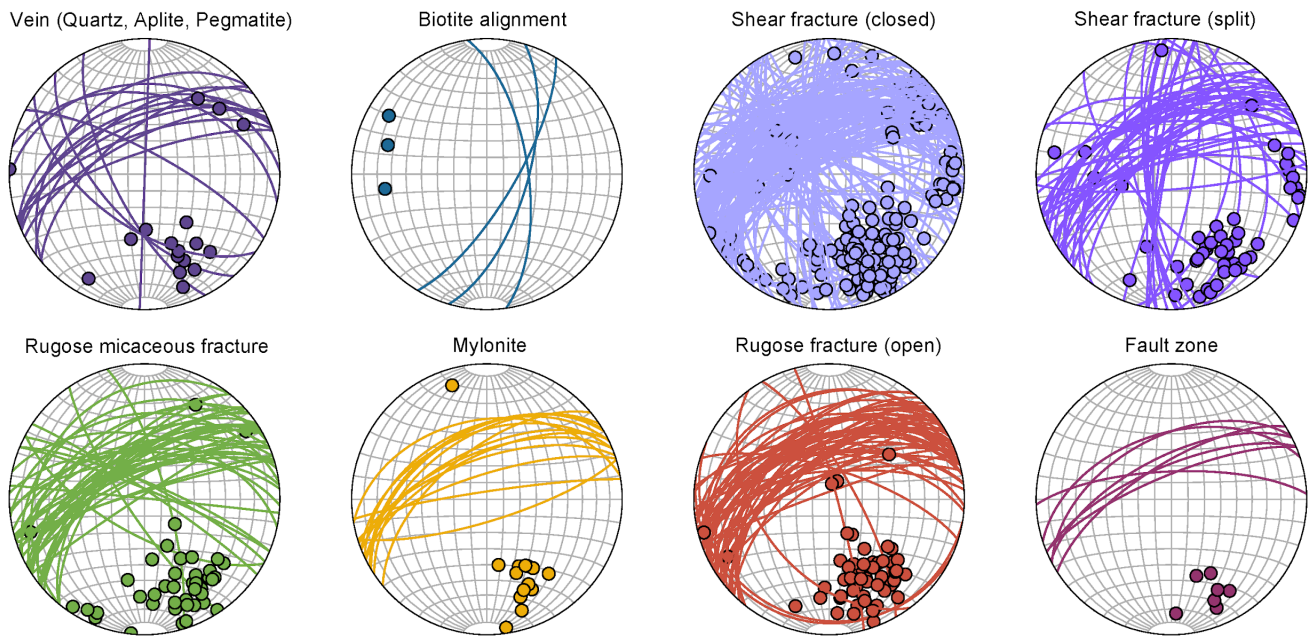
b)

55

56 **Figure 6: a) Core images, compositions and the structure of the major fault zone encountered in borehole CB1 (between 143-145 m**
 57 **measured depth). Ductile and brittle structures can be seen in close proximity to each other. Brittle structures are located at the**
 58 **boundaries of ductile features; b) Schematics of the fault zone structure.**

59

60

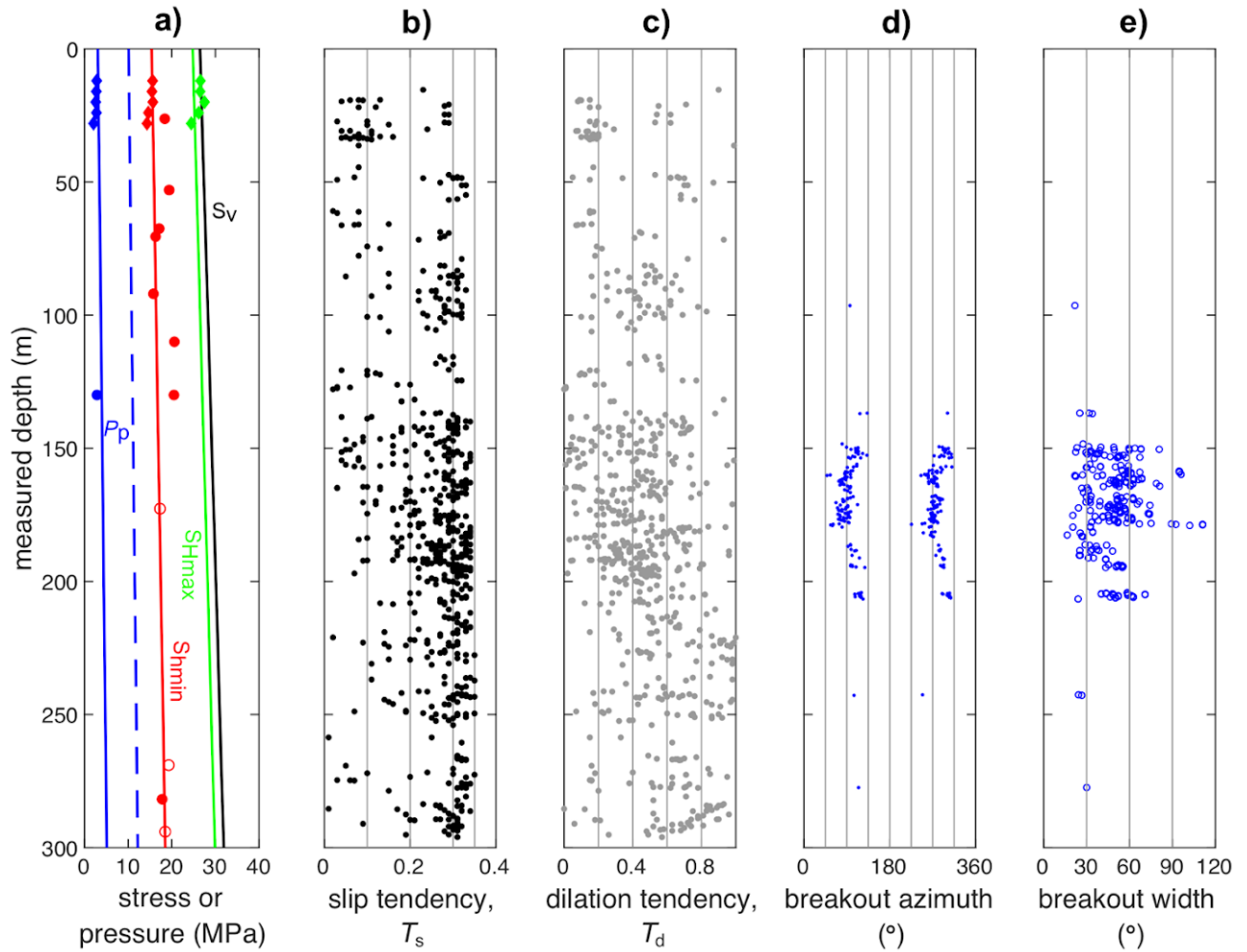


62

63 **Figure 7: Mapped geological structures by type. The upper row shows the orientation of structures that are mainly ‘closed’ (based**
 64 **on visual examination of the cores). The lower row shows the orientations of structures with higher shear strain and can be perceived**
 65 **as ‘open’. Note the structures shown in the lower row are almost exclusively oriented NE-SW.**

66

67



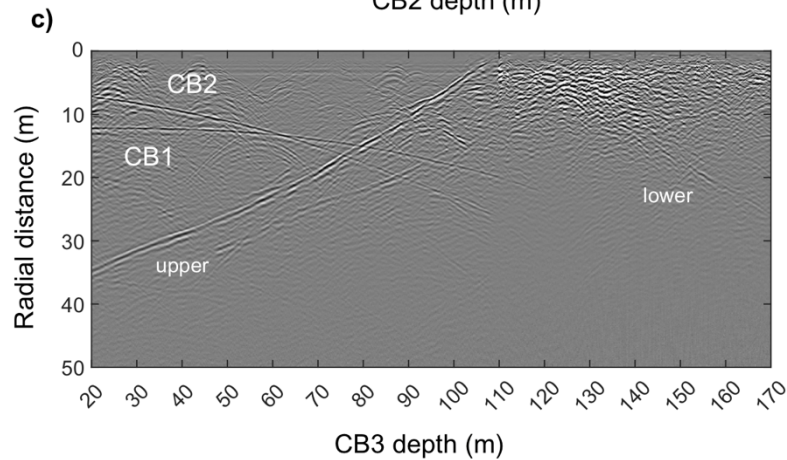
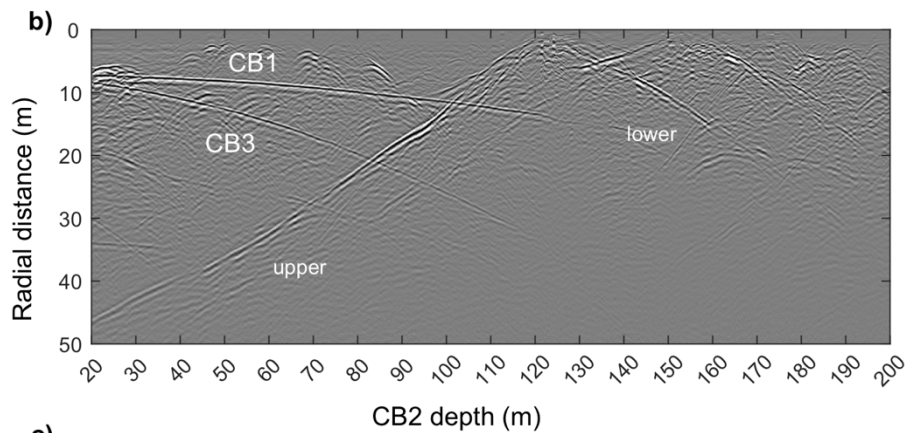
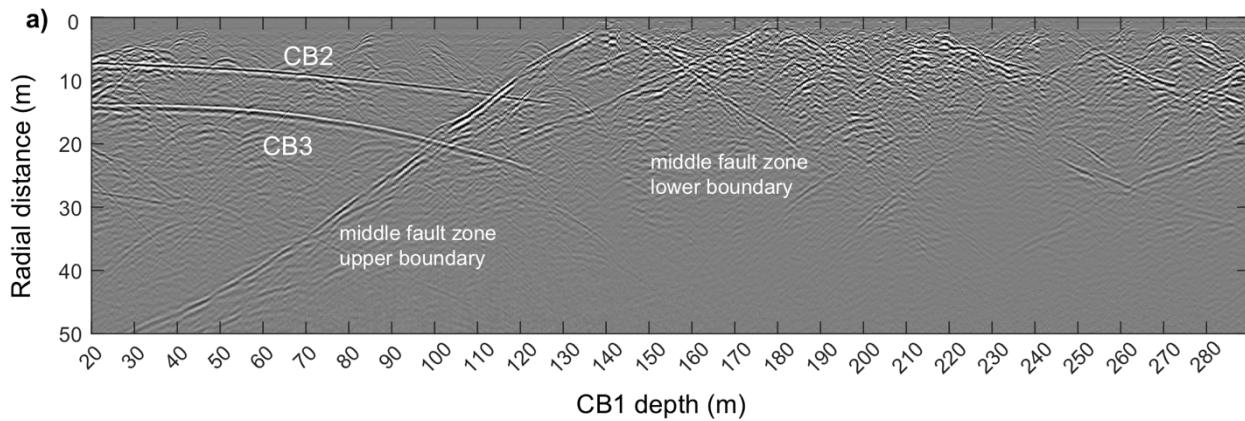
68

69 **Figure 8: Integrated geomechanical information of borehole CB1: a) stress and pore pressure profiles (Diamonds are from SB**
 70 **borehole data; circles are from CB1, while open circles are of uncertainty; dashed blue gradient represents hydrostatic pore**
 71 **pressure.); b) slip tendency (T_s) and c) dilation tendency (T_d) of all mapped structures (shown in Figure 5); d) breakout azimuths**
 72 **and c) widths (0° refers to the high-side of the borehole).**

73

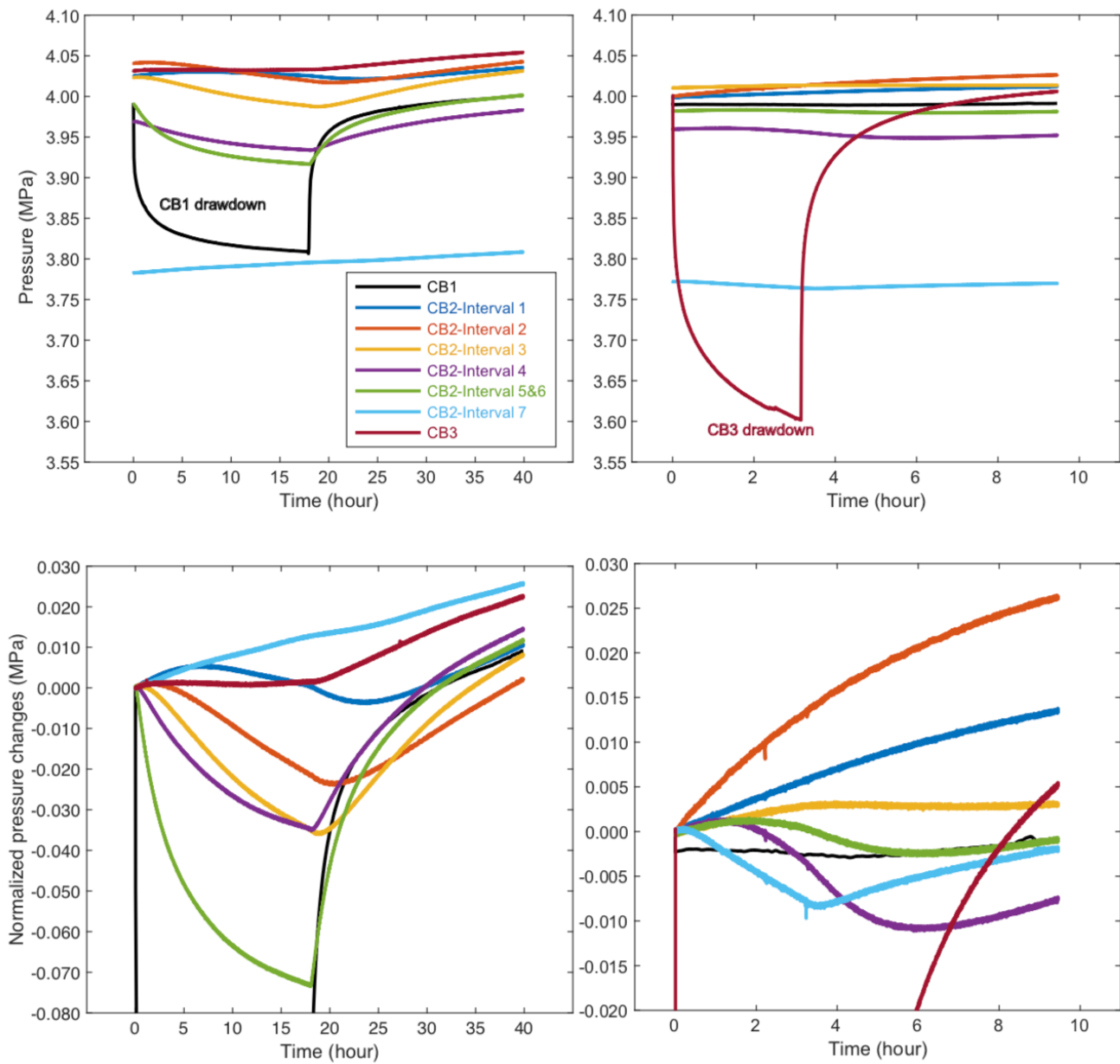
74

75



76

77 **Figure 9: Single-hole GPR reflection profiles (100 MHz) along: a) CB1, b) CB2, and c) CB3. From each borehole, the nearby**
 78 **boreholes are identified (and labelled) as prominent reflectors. The middle unit of the first major fault zones is clearly dominant in**
 79 **the figure. The fractured rock below this fault zone is characterized by higher reflectivity. Above the fault zone, some parabolic**
 80 **reflectors are seen that are likely attributed to borehole-perpendicular fractures.**



81
82
83
84
85

Figure 10: The pressure response of boreholes/intervals to the drawdown in CB1 (left) and CB3 (right). The upper and lower row present the absolute and relative pressure (changes), respectively.